

# Roles of vertical distributions of atmospheric transient eddy dynamical forcing and diabatic heating in midlatitude unstable air-sea interaction

Jiabei Fang

Nanjing University

Lilan Chen

Nanjing University

Xiu-Qun Yang (✉ [xqyang@nju.edu.cn](mailto:xqyang@nju.edu.cn))

Nanjing University <https://orcid.org/0000-0003-3716-9152>

---

## Original Article

**Keywords:** Midlatitude air-sea interaction, diabatic heating, transient eddy vorticity forcing, baroclinic atmosphere model

**Posted Date:** February 9th, 2021

**DOI:** <https://doi.org/10.21203/rs.3.rs-198305/v1>

**License:**  This work is licensed under a Creative Commons Attribution 4.0 International License.

[Read Full License](#)

---

**Version of Record:** A version of this preprint was published at Climate Dynamics on August 9th, 2021. See the published version at <https://doi.org/10.1007/s00382-021-05912-8>.

1       **Roles of vertical distributions of atmospheric transient eddy**  
2       **dynamical forcing and diabatic heating in midlatitude unstable**  
3       **air-sea interaction**

4  
5                   Jiabei Fang, Lilan Chen, Xiu-Qun Yang

6       *CMA-NJU Joint Laboratory for Climate Prediction Studies, School of Atmospheric*  
7                   *Sciences, Nanjing University, Nanjing, China*

8  
9  
10                  Correspondence to:

11                   Dr. Xiu-Qun Yang, *xqyang@nju.edu.cn*,

12                   Dr. Jiabei Fang, *fangjb@nju.edu.cn*

13  
14

## Abstract

Atmospheric transient eddy dynamical forcing (TEDF)-driven midlatitude unstable air-sea interaction has recently been recognized as a crucial positive feedback for the maintenance of the extratropical decadal variabilities. Our previous theoretical work by Chen et al. (2020) characterizes such an interaction with building an analytical midlatitude barotropic atmospheric model coupled to a simplified upper oceanic model. This study firstly extends the analytical model to a two-layer quasi-geostrophic baroclinic atmospheric model coupled to a simplified upper oceanic model and then identifies the roles of vertical distributions of atmospheric TEDF and diabatic heating in midlatitude unstable air-sea interaction. It is found that the midlatitude air-sea coupling through atmospheric TEDF and diabatic heating with more realistic vertical profile destabilizes the oceanic Rossby wave mode over the entire range of zonal wavelengths, and the most unstable mode exhibits an equivalent barotropic structure with geopotential lows (highs) over cold (warm) water. The spatial configuration structure and period of the most unstable coupled mode are more consistent with the observation than those from the previous model. Although either TEDF or diabatic heating alone can lead to unstable air-sea interaction, the former is dominant to the instability. TEDF in both higher and lower layers can cause unstable coupled mode individually, while the lower-layer forcing stimulates instability more effectively. Surface diabatic heating always destabilizes the coupled mode, while the mid-level heating always decays the coupled mode. Moreover, the influences of oceanic adjustment processes, air-sea coupling strength and background zonal wind on the unstable coupled mode are also discussed. The results of this study further prove the TEDF-driven positive feedback mechanism in midlatitude air-sea interaction proposed by recent observational and numerical experiment studies.

Keywords: Midlatitude air-sea interaction, diabatic heating, transient eddy vorticity forcing, baroclinic atmosphere model

## 42 **1 Introduction**

43 Observational studies have revealed that there is a significant decadal variability in the  
44 midlatitude North Pacific ocean–atmosphere system (Trenberth 1990; Graham et al.  
45 1994; Minobe 1997; Mantua et al. 1997; Enfield and Mestas-Nunez 1999; Zhu and  
46 Yang 2003; Fang et al. 2006). The decadal mode of North Pacific SST anomalies, also  
47 known as the Pacific Decadal Oscillation (PDO), is well correlated with the  
48 atmospheric circulation anomalies that exhibit an equivalent barotropic structure in the  
49 vertical direction, with geopotential lows (highs) above cold (warm) water (Kushnir et  
50 al. 2002; Namias and Cayan 1981; Fang and Yang 2016). Such an equivalent barotropic  
51 cold/ trough (warm/ridge) structure is also the typical feature of midlatitude climate  
52 variabilities on decadal time scale (Cayan 1992; Deser and Blackman 1993).

53 As we know, to generate an oscillation, a positive feedback mechanism is needed  
54 to make the initial perturbation develop, and a delayed negative feedback mechanism  
55 is also needed to make the anomalous phase transition. For PDO, the negative feedback  
56 mechanism is thought to be the slow upper-ocean adjustment processes involving the  
57 oceanic gyre (Latif and Barnett 1994; Fang et al. 2006), the subduction (Gu and  
58 Philander 1997), and the oceanic Rossby wave propagation (Qiu et al. 2007). The  
59 decadal time scale of PDO is determined by the adjustment period. While the positive  
60 feedback mechanism is considered to be the local large-scale ocean-atmosphere  
61 interaction in the middle latitudes (Latif and Barnett 1994, 1996; Latif 1999; Miller and  
62 Schneider 2000; Robertson 1996; Zorita and Frankignoul 1997). Though a number of  
63 observations, theoretical analyses and GCM simulations have provided evidence for the  
64 active feedback of extratropical SST on large-scale atmospheric circulation (Saravanan  
65 and McWilliams 1997, 1998; Neelin and Weng 1999; Latif and Barnett 1996; Liu and  
66 Wu 2004; Zhong et al. 2008; Zhu et al. 2008; Fang and Yang 2011), the mechanism  
67 responsible for the midlatitude air-sea interaction remains unclear for a long time. It is

68 primarily because the processes by which the midlatitude sea surface temperature (SST)  
69 anomaly affects the seasonal-mean atmospheric anomaly has not been fully understood.

70 Different from the tropical atmospheric circulation that is mainly driven by the  
71 SST-induced convective diabatic heating, the midlatitude atmospheric circulation is  
72 both thermally- and eddy-driven. Since the atmospheric stratification in the middle  
73 latitudes is stable, the SST-induced diabatic heating, mostly through sensible heat  
74 transportation and latent heat release, is relatively weak and mainly confined to the  
75 lower troposphere. On the other hand, the midlatitude atmosphere is strongly baroclinic,  
76 and the synoptic transient eddies are the most active over midlatitude oceans,  
77 particularly over the midlatitude oceanic frontal zones, forming stormtracks (Ren et al.  
78 2010; Chu et al. 2013; Liu et al. 2014; Nakamura et al. 2004; Small et al. 2008; Wang  
79 et al. 2017). The nonlinear interaction of transient eddies can systematically transport  
80 heat and momentum, driving and maintaining atmospheric circulations in the middle  
81 latitudes (Ren et al. 2011; Xiang and Yang 2012; Zhang et al. 2012; Nie et al. 2013,  
82 2014). From the perspective of quasi-geostrophic potential vorticity (QGPV) dynamics,  
83 the seasonal-mean PV sources include the diabatic heating, the transient eddy heating,  
84 and the transient eddy vorticity forcing (Lau and Holopainen 1984; Fang and Yang  
85 2016). The latter two items that are caused by the convergence of the heat and vorticity  
86 transport by transient eddies, respectively, can be considered as indirect forcing sources  
87 of atmospheric circulation. Therefore, the midlatitude SST anomalies can affect the  
88 atmosphere by changing both the diabatic heating and the transient eddy forcing.

89 Fang and Yang (2016) identified the distribution features of the PDO-related  
90 atmospheric forcing terms and quantitatively diagnosed their effect on the atmosphere.  
91 Based on these analyses, a hypothesis on the positive feedback mechanism for  
92 midlatitude unstable air-sea interaction in the North Pacific was further proposed. An  
93 initial midlatitude surface westerly anomaly accompanied with intensified Aleutian low  
94 tends to force a negative SST anomaly by increasing upward surface heat fluxes and

95 driving southward Ekman current anomaly. Then, the basin-scale SST cooling tends to  
96 increase the meridional SST gradient in its southern flank, thus enhancing the  
97 subtropical oceanic front. As an adjustment to the enhanced oceanic front, the low-level  
98 atmospheric baroclinicity tends to be strengthened, and more transient eddies are  
99 generated, resulting in more meridional thermal and momentum transportation.  
100 Although all the diabatic heating, transient eddy heating and transient eddy vorticity  
101 forcing are increased during these processes, only the atmospheric response to the  
102 transient eddy vorticity forcing tends to be barotropic. The vorticity forcing that  
103 dominates the total atmospheric forcing tends to produce an equivalent barotropic  
104 atmospheric low pressure that intensifies the initial anomalies of the midlatitude surface  
105 westerly and Aleutian low. Therefore, the midlatitude ocean–atmosphere interaction, in  
106 which the oceanic front and the atmospheric transient eddy are the indispensable  
107 ingredients, can provide a positive feedback mechanism for the development and  
108 maintenance of the observed decadal anomalies in the midlatitude North Pacific ocean–  
109 atmosphere system. This hypothesis has also been confirmed by the later observational  
110 and numerical simulation studies (Wang et al., 2017; Wang et al. 2019; Tao et al. 2020;  
111 Zhang et al. 2020).

112 Since the transient eddy dynamical feedback is an important process for the ocean  
113 to influence the atmosphere, in our recent work (Chen et al, 2020, hereinafter  
114 CYF2020), an analytical coupled air-sea model including atmospheric vorticity forcing  
115 is established to investigate its contribution to midlatitude unstable air-sea interaction.  
116 The transient eddy vorticity forcing is parameterized to be linearly proportional to the  
117 meridional second-order derivative of SST on the base of observational analyses.  
118 Considering the prominent characteristics of the equivalent barotropic structure of the  
119 midlatitude atmospheric circulation, for simplicity, the atmospheric model is assumed  
120 to be barotropic. It is found that the oceanic Rossby wave stimulated by air-sea coupling  
121 can be unstable within a wide range of wavelengths. The configuration structure of the

122 most unstable mode is similar to that of the observed decadal variability. Although both  
123 surface diabatic heating and transient eddy vorticity forcing can cause unstable mode,  
124 the latter plays a dominant role. This results also provide theoretical support for the  
125 midlatitude ocean-atmosphere interaction hypothesis.

126 However, in the previous theoretical research, the assumption of barotropic  
127 atmosphere is simple. Actually, both diabatic heating and transient eddy vorticity  
128 forcing have vertical variations. Some studies using linear baroclinic model show that  
129 the atmospheric response is sensitive to the vertical structure of the idealized heat  
130 source. To low-level heating, the atmosphere tends to produce a barotropic low-  
131 pressure response, while to the mid-level heat source, the atmospheric response tends  
132 to be baroclinic (Qiu et al. 2014; Hoskins and Karoly 1981; Fang and Yang 2011).  
133 Moreover, the influence of vertical distribution of the transient eddy vorticity forcing  
134 on the atmospheric response is still unclear.

135 Therefore, in the present study, the atmospheric component of the analytical  
136 midlatitude coupled air-sea model in CYF2020 is extended to a two-layer baroclinic  
137 quasi-geostrophic model, and the oceanic component remains a one and a half-layer  
138 upper ocean model. The vertical structures of diabatic heating and transient eddy  
139 vorticity forcing are both taken into account to further explore their relative  
140 contributions to midlatitude unstable ocean-atmosphere interaction. The paper is  
141 organized as follows. Description of the analytical coupled model are presented in  
142 Section 2. The dynamical features of midlatitude air-sea coupled mode and the relative  
143 contributions of diabatic heating and transient eddy vorticity forcing with difference  
144 vertical profiles are examined in Section 3 and Section 4, respectively. Comparison  
145 with the results of barotropic model is presented in Section 5. Influence of other  
146 processes and factors on unstable coupled mode such as the oceanic adjustment  
147 processes, the air-sea coupling intensity and the background atmospheric flow are  
148 discussed in Section 6. The final section is devoted to the conclusions and discussion.

149 **2. An extended analytical midlatitude coupled air-sea model**

150 Figure 1 shows the diagram of the extended analytical coupled model used in this study.  
 151 The atmospheric component is described by a two-layer baroclinic quasi-geostrophic  
 152 model with a shallow boundary layer. The oceanic component remains a quasi-  
 153 geostrophic upper-ocean model, as in CYF2020, which consists of a constant-depth  
 154 mixed layer, a thin entrainment layer and a thermocline layer. Both the atmosphere and  
 155 ocean are governed by their respective quasi-geostrophic potential vorticity (QGPV)  
 156 equations on a midlatitude beta plane.

157 For the atmosphere, the diabatic heating is imagined to occur both at the top of  
 158 boundary layer (surface heating,  $Q_s$ ) and between the two layers (mid-level  
 159 heating,  $Q$ ). The transient eddy vorticity forcing ( $F_{eddy}$ ) exists in both layers. Since the  
 160 adjustment time scale of the atmosphere is much shorter than that of the ocean, the  
 161 atmospheric fluctuations are assumed to be a steady-state response to the forcing  
 162 sources. Therefore, the seasonal mean QGPV equations for the two atmospheric layers  
 163 can be written as

164 
$$J(\bar{\psi}_1, \bar{q}_1) + r\nabla^2\bar{\psi}_1 = \bar{F}_{eddy1} - \frac{gH_a\bar{Q}}{2fL_a^2} \quad \text{and} \quad (1)$$

165 
$$J(\bar{\psi}_2, \bar{q}_2) + r\nabla^2\bar{\psi}_2 = \bar{F}_{eddy2} + \frac{gH_a(\bar{Q}-\bar{Q}_s)}{2fL_a^2},$$
  
 166 (2)

167 where the overbar denotes seasonal mean,  $q$  is the potential vorticity defined by

168 
$$\bar{q}_1 = \nabla^2\bar{\psi}_1 + \beta y -$$

169 
$$\frac{1}{L_a^2}(\bar{\psi}_1 - \bar{\psi}_2) \quad \text{and} \quad (3)$$

170 
$$\bar{q}_2 = \nabla^2\bar{\psi}_2 + \beta y + \frac{1}{L_a^2}(\bar{\psi}_1 - \bar{\psi}_2) \quad ,$$

171 (4)

172  $\psi$  is the stream function,  $J(a, b) = \frac{\partial a}{\partial x} \frac{\partial b}{\partial y} - \frac{\partial a}{\partial y} \frac{\partial b}{\partial x}$  is the Jacobi operator,  $L_a =$

173  $(N_a H_a)/(2f)$  is the atmospheric baroclinic Rossby radius of deformation with  $N_a$

174 the atmospheric Brunt–Väisälä buoyancy frequency, and  $H_a$  is the depth of the free  
 175 troposphere. According to the equations, the seasonal mean atmospheric circulation is  
 176 driven by both diabatic heat forcing (the second term on the right hand) and transient  
 177 eddy vorticity forcing ( $\bar{F}_{eddy}$ ). The former term is proportional to the vertical gradient  
 178 of diabatic heating, while  $\bar{F}_{eddy} = -\nabla \cdot \overline{\bar{V}'_h \zeta'}$  represents the seasonal mean vorticity  
 179 transportation by synoptic transient eddies (denoted by primes).  $r\nabla^2 \bar{\psi}$  indicates the  
 180 damping effect that is proportional to the relative vorticity, and  $r$  is the diffusive  
 181 coefficient with the characteristic time scale  $r^{-1} = 5$  days (Pedlosky 1970).

182 If we simply suppose that the basic state is horizontally uniform zonal flow with  
 183 vertical shear, the seasonal mean atmospheric streamfunction can be expressed as the  
 184 sum of a basic flow (climatological mean) and a perturbation (seasonal anomaly) like  
 185  $\bar{\psi}_1 = \psi_1 - U_1 y$ ,  $\bar{\psi}_2 = \psi_2 - U_2 y$ . Further decomposing the atmospheric circulation  
 186 into barotropic and baroclinic components by defining

$$187 \quad \hat{\psi} = \psi_1 + \psi_2; \quad \tilde{\psi} = \psi_1 - \psi_2 \quad (5)$$

$$188 \quad \hat{U} = U_1 + U_2; \quad \tilde{U} = U_1 - U_2, \quad (6)$$

189 we can derive the linearized barotropic and baroclinic PV perturbation equations as

$$190 \quad \hat{U} \frac{\partial}{\partial x} \nabla^2 \hat{\psi} + \hat{\beta} \frac{\partial \hat{\psi}}{\partial x} + \tilde{U} \frac{\partial}{\partial x} \nabla^2 \tilde{\psi} + 2r \nabla^2 \hat{\psi} = 2F_{eddy1} + 2F_{eddy2} - \frac{gH_a Q_s}{fL_a^2}$$

191 (7)

$$192 \quad \hat{U} \frac{\partial}{\partial x} \left\{ \nabla^2 \tilde{\psi} - \frac{2}{L_a^2} \tilde{\psi} \right\} + \tilde{\beta} \frac{\partial \tilde{\psi}}{\partial x} + \tilde{U} \frac{\partial}{\partial x} \nabla^2 \hat{\psi} + \hat{\beta} \frac{\partial \hat{\psi}}{\partial x} + 2r \nabla^2 \tilde{\psi} =$$

$$193 \quad 2F_{eddy1} - 2F_{eddy2} - \frac{2gH_a Q}{fL_a^2} + \frac{gH_a Q_s}{fL_a^2}, \quad (8)$$

194 where  $\hat{\beta} = 2\beta$ ,  $\tilde{\beta} = 2\tilde{U}/L_a^2$ . It should be noted that the surface diabatic heating and  
 195 the atmospheric transient eddy vorticity forcing in each layer drive the barotropic and  
 196 baroclinic components together, whereas the mid-level heating only acts on the  
 197 baroclinic component.

198 As documented in CYF2020, the anomalous transient eddy vorticity forcing is  
 199 proportional to the meridional second order derivative of SST anomaly. Thus here the  
 200 vorticity forcing in the upper layer is specified equal to that in the barotropic coupled  
 201 model (CYF2020) given by  $F_{eddy1} = \gamma \partial^2 T_1 / \partial y^2$ , with  $T_1$  the sea surface  
 202 temperature anomaly. Meanwhile, following Fang and Yang (2011) as well as Shutts  
 203 (1987), the mid-level heating is prescribed to have the form of Newtonian relaxation of  
 204 the atmospheric potential temperature perturbation at middle level  $\theta_a$  to a radiative–  
 205 convective equilibrium temperature anomaly  $\theta_a^*$ , given by

$$206 \quad Q = -\gamma_a \left( \frac{\theta_a}{\theta_{ao}} - \frac{\theta_a^*}{\theta_{ao}} \right) = -\gamma_a \left( \frac{2f}{gH_a} \tilde{\psi} - \frac{\theta_a^*}{\theta_{ao}} \right). \quad (9)$$

207 Here  $\theta_a$  has been converted to  $\tilde{\psi}$  using the thermal wind relation,  $\theta_{ao}$  is a typical  
 208 value of  $\theta_a$ ,  $\gamma_a$  is the atmospheric air–sea heat exchange parameter, and  $\theta_a^*$  is set to  
 209 be the function of SST anomaly. For simplicity, it is assumed that  $\theta_a^* = T_1$ .

210 Based on the observational analysis on the vertical distribution of the anomalous  
 211 diabatic heating and transient eddy vorticity forcing in North Pacific region (Fig. 2b  
 212 and c, quoted from CYF2020), the surface heating is estimated to be twice as large as  
 213 that of mid-level heating ( $Q_s = \gamma_2 Q$ ,  $\gamma_2 = 2$ ), and the transient eddy vorticity forcing  
 214 in the lower atmosphere is estimated to be 0.2 times of that in the upper atmosphere  
 215 ( $F_{eddy2} = \delta_2 F_{eddy1}$ ,  $\delta_2 = 0.2$ ). Hence the atmospheric equations (7)-(8) can be  
 216 rewritten as

$$217 \quad \hat{U} \frac{\partial}{\partial x} \nabla^2 \hat{\psi} + \hat{\beta} \frac{\partial \hat{\psi}}{\partial x} + \tilde{U} \frac{\partial}{\partial x} \nabla^2 \tilde{\psi} + 2r \nabla^2 \hat{\psi} \\
 218 \quad = 2\gamma(1 + \delta_2) \frac{\partial^2 T_1}{\partial y^2} + \frac{2\gamma_a \gamma_2}{L_a^2} \left( \tilde{\psi} - \frac{1}{r_a} T_1 \right) \quad (9)$$

$$219 \quad \hat{U} \frac{\partial}{\partial x} \left\{ \nabla^2 \tilde{\psi} - \frac{2}{L_a^2} \tilde{\psi} \right\} + \tilde{\beta} \frac{\partial \tilde{\psi}}{\partial x} + \tilde{U} \frac{\partial}{\partial x} \nabla^2 \hat{\psi} + \hat{\beta} \frac{\partial \tilde{\psi}}{\partial x} + 2r \nabla^2 \tilde{\psi} \\
 220 \quad = 2\gamma(1 - \delta_2) \frac{\partial^2 T_1}{\partial y^2} + \frac{2\gamma_a(2 - \gamma_2)}{L_a^2} \left( \tilde{\psi} - \frac{1}{r_a} T_1 \right), \quad (10)$$

221 Where  $r_a \equiv (2f\theta_{ao})/(gH_a)$ .

222 The oceanic component of the coupled model remains the same as in CYF2020  
 223 and in Fang and Yang (2011). The upper-layer motion represented by the first  
 224 baroclinic Rossby mode is controlled by a linear QGPV equation with a rest basic state  
 225 driven by the curl of the surface wind stress. The evolution of SST is determined by the  
 226 physical processes including horizontal advection, vertical entrainment and heat  
 227 exchange at air-sea interface. The governing equations are given by

$$228 \quad -\frac{1}{L_o^2} \frac{\partial \psi_o}{\partial t} + \beta \frac{\partial \psi_o}{\partial x} = \alpha \nabla^2 (\hat{\psi}/2 - \tilde{\psi})$$

229 (11)

$$230 \quad \frac{\partial T_1}{\partial t} = c_1 \psi_o - c_2 T_1 - c_3 W_e + c_4 \frac{\partial \psi_o}{\partial x} + c_4 \frac{H-H_1}{H} v_s - \gamma_o (T_1 - r_a \tilde{\psi}), \quad (12)$$

231 where  $\psi_o$  is the upper-layer oceanic geostrophic streamfunction,  $L_o$  is the oceanic  
 232 baroclinic Rossby radius of deformation,  $c_1, c_2, c_3$  and  $c_4$  are all positive coefficients  
 233 relevant to advection and entrainment processes, and  $\gamma_o$  is the oceanic air-sea heat  
 234 exchange parameter.

235 Therefore, equations (9)-(12) constitute the final closed equations for the coupled  
 236 ocean-atmosphere model. Compared with the coupled model used in Fang and Yang  
 237 (2011), the mechanism of transient eddy dynamical feedback is introduced in the  
 238 present model. Also, the coupled model with barotropic atmosphere in CYF2020 can  
 239 be regarded as a special case of the present model.

### 240 **3. Features and dynamics of the unstable midlatitude coupled modes**

241 The perturbations of the atmospheric and oceanic variables are assumed to be limited  
 242 within a  $[0, \pi]$  channel in  $Y$  direction, and to satisfy the standard plane wave solution  
 243 in  $X$  direction with the form

$$244 \quad (\hat{\psi}, \tilde{\psi}, \psi_o, T_1) = (\hat{\psi}'', \tilde{\psi}'', \psi_o'', T_1'') e^{i(kx - \sigma t)} \text{sinly}. \quad (13)$$

245 Here  $\hat{\psi}'', \tilde{\psi}'', \psi_o''$  and  $T_1''$  are the amplitudes of these variables,  $\sigma$  is the complex  
 246 frequency,  $k$  and  $l$  are the horizontal wavenumbers in  $x$  and  $y$  directions,

247 respectively. Inserting (13) into equations (9)-(12), we can obtain the following  
 248 dispersion relations of the coupled modes:

$$\begin{aligned}
 249 \quad \sigma_{\pm} = & \frac{1}{2} \left\{ \omega_r - ic_2 - i\gamma_o + \frac{\left[ 2\gamma l^2(1+\delta_2) + \frac{2\gamma_a\gamma_2}{L_a^2} \frac{1}{ra} \right] \left[ \gamma_o r_a - [c'_3 f K^2 + c'_4 (r_s k + fl) i] \frac{\alpha(\frac{\mu}{2}+1)}{(f^2+r_s^2)} \right]}{\mu k \left( -\bar{U} K^2 + \hat{\beta} - \frac{2rK^2}{ik} \right) + \bar{U} k K^2 + \frac{2\gamma_a\gamma_2}{L_a^2} i} \right\} \\
 250 \quad & \pm i \left\{ -\frac{1}{4} (\omega_r + ic_2 + i\gamma_o - \frac{\left[ 2\gamma l^2(1+\delta_2) + \frac{2\gamma_a\gamma_2}{L_a^2} \frac{1}{ra} \right] \left[ \gamma_o r_a - [c'_3 f K^2 + c'_4 (r_s k + fl) i] \frac{\alpha(\frac{\mu}{2}+1)}{(f^2+r_s^2)} \right]}{\mu k \left( -\bar{U} K^2 + \hat{\beta} - \frac{2rK^2}{ik} \right) + \bar{U} k K^2 + \frac{2\gamma_a\gamma_2}{L_a^2} i})^2 - (c_1 + \right. \\
 251 \quad & \left. c_4 ik) \frac{\alpha K^2 L_0^2 (\frac{\mu}{2}+1) \left[ 2\gamma l^2(1+\delta_2) + \frac{2\gamma_a\gamma_2}{L_a^2} \frac{1}{ra} \right]}{\left[ \mu ik \left( -\bar{U} K^2 + \hat{\beta} - \frac{2rK^2}{ik} \right) + \bar{U} ik K^2 + \frac{2\gamma_a\gamma_2}{L_a^2} \right]} \right\}^{\frac{1}{2}}, \quad (14)
 \end{aligned}$$

252 where  $\omega_r \equiv -k\beta L_0^2$  is the frequency of free oceanic baroclinic Rossby wave,  $K^2 =$   
 253  $k^2 + l^2$  represents the square of total wavenumber,  $c'_3 = c_3(H - H_1)$  and  $c'_4 =$   
 254  $c_4(H - H_1)/H_1$  are both positive coefficients, and

$$\begin{aligned}
 255 \quad \mu = & \frac{\bar{U} K^2 + \bar{U} K_a^2 - \hat{\beta} + \frac{2rK^2}{ik} + \frac{2\gamma l^2 L_a^2 r a}{\gamma_a \gamma_2} \left( -\bar{U} K_a^2 + \hat{\beta} - \frac{2rK^2}{ik} + \frac{2\gamma_a\gamma_2}{L_a^2 ik} \right)}{\bar{U} K^2 - \hat{\beta} + \frac{2rK^2}{ik} + \bar{U} K^2 - \hat{\beta} + \frac{2\gamma l^2 L_a^2 r a}{\gamma_a \gamma_2} (-\bar{U} K^2 + \hat{\beta})} \\
 256 \quad & (15)
 \end{aligned}$$

257 measures the relative strength of barotropic and baroclinic modes as  $\hat{\psi} = -\mu\tilde{\psi}$ .

258 The two solutions of (14) corresponds to two coupled modes caused by midaltitude  
 259 air–sea interaction. The real part of  $\sigma$  represents the frequency of the coupled mode  
 260 and the imaginary part indicates the growth rate of the amplitude of coupled mode.  
 261 Therefore, the coupled mode will be unstable if the imaginary part of  $\sigma$  is positive.  
 262 Given the same parameter values as in CYF2020 (see Table 1), except that the basic  
 263 zonal wind for upper and lower atmosphere are  $U_1 = 17ms^{-1}$  and  $U_2 = 8ms^{-1}$   
 264 respectively. The frequency and growth rate of the two coupled modes can be calculated  
 265 as a function of zonal wavelength. The frequency curve of the first mode (the blue line  
 266 in Fig.3a) is very close to that of the free oceanic Rossby wave (the red line), thus the  
 267 first coupled mode ( $\sigma_+$ ) is essentially a coupled oceanic Rossby wave mode modified  
 268 by air–sea interaction. The coupled oceanic Rossby wave propagates westward and  
 269 destabilizes over the whole range of wavelengths (Fig. 3b). The other coupled mode

270 ( $\sigma_-$ ) corresponds to a eastward-propagating decay mode since its growth rate is always  
271 negative within entire zonal wavelengths (Figure not shown). Because our focus in this  
272 study is mainly on the unstable air–sea interaction, the damping mode will no longer be  
273 discussed in the following part.

274 The most unstable coupled Rossby wave mode occurs at the wavelength around  
275 9900km (Fig. 3b). Its corresponding frequency is -0.7765 per year (Fig. 3a) and thus  
276 the period is nearly 8 years, close to that of the observed decadal variability. Figure 4  
277 shows the spatial phase relationships between the SST anomaly (shaded) and the upper-  
278 and lower-layer atmospheric streamfunction as well as upper-oceanic streamfunction  
279 anomalies (contours) for the most unstable coupled mode. It can be found that the  
280 upper- and lower-layer atmospheric streamfunction anomalies are both in phase with  
281 the SST anomaly, indicating that the atmospheric response to the SST anomaly is  
282 equivalent barotropic with highs (lows) over warm (cold) water (Fig. 4a and 4b). In  
283 addition, the wind-driven upper oceanic streamfunction anomaly has a small eastward  
284 phase shift relative to SST and atmospheric streamfunction anomalies, mainly due to  
285 the advection process. Such configuration relationship between atmospheric and  
286 oceanic anomalies is also consistent with that of the observed decadal variability. Hence,  
287 it is suggested that midlatitude ocean-atmosphere interaction through thermal and  
288 transient eddy dynamical feedback can produce a coupled oceanic Rossby wave mode  
289 on decadal time scale with equivalent barotropic cold trough/warm ridge structure.

290 Compared with the results of CYF2020 in which the atmosphere is assumed to be  
291 barotropic, the period of the most unstable mode becomes longer, and the associated  
292 anomalous SST and atmospheric streamfunction are exactly in phase like observation  
293 instead of having a small phase shift in  $x$  direction (Fig.5). However, the unstable  
294 growth rate is reduced by more than half (Fig. 11a). The differences between the two  
295 works and the causing reasons will be discussed in detail in Section 5.

## 296 **4. Roles of diabatic heating and atmospheric transient eddy vorticity forcing**

### 297 **4.1 Role of diabatic heating with different vertical profiles**

298 In this coupled model, diabatic heat forcing and atmospheric transient eddy vorticity  
299 forcing are the two PV sources that jointly affect the seasonal-mean atmospheric  
300 circulation anomaly. To examine the relative contributions of different PV sources in  
301 destabilizing the coupled oceanic Rossby wave mode, the transient eddy vorticity  
302 forcing term is firstly removed by setting  $\gamma = 0$  in equations (9) and (10). Three cases  
303 with different heating profiles are investigated, respectively: surface heating only case  
304 ( $Q_s \neq 0, Q = 0$ ), mid-level heating only case ( $Q_s = 0, Q \neq 0$ ) and both surface and  
305 mid-level heating case ( $Q_s, Q \neq 0$ ).

306 The dispersion relation curves of all the three cases are basically the same as  
307 shown in Fig. 6a, 6c and 6e, coinciding with that of the free oceanic Rossby wave.  
308 When the surface heating is considered alone, the coupled oceanic Rossby mode also  
309 destabilizes over the entire wavelength range (Fig. 6b), but its growth rate decreases  
310 significantly compared with the standard case (full PV sources case, Fig. 3b) and the  
311 most unstable mode shifts to shorter wavelength at around 8500km. However, if the  
312 mid-level heating is added alone, the coupled oceanic Rossby mode becomes a weak-  
313 damping mode. Comparing the phase relationships of atmospheric and oceanic  
314 variables for the two cases (Fig. 7), we can find that the atmospheric responses for the  
315 two cases are nearly opposite. To surface cooling induced by cold SST anomaly, the  
316 atmospheric response shows an equivalent barotropic lows above cold water anomaly  
317 (Fig. 7a and c), similar as in the standard case but with a eastward phase shift relative  
318 to SST anomalies. The surface low pressure can sustain the cyclonic oceanic flow and  
319 enhance the cold SST anomaly by transporting cold water (Fig. 7e), forming a positive  
320 feedback. Thus the stimulated coupled Rossby wave mode is a growing mode. Whereas  
321 to the SST induced mid-level cooling, the upper atmospheric streamfunction has an in-

322 phase high anomaly response (Fig. 7b), and the lower atmospheric streamfunction  
323 anomaly leads that of the upper layer by nearly  $\pi/2$  phase (Fig. 7d). The surface high  
324 pressure will weaken the cyclonic oceanic flow and thus reduce the cold SST anomaly.  
325 Therefore, the coupled Rossby wave mode decays gradually.

326 When the surface and mid-level heating are both included, the results are very  
327 similar to that of the surface heating only case (Fig. 6f), indicating that the contribution  
328 of diabatic heating to the unstable air-sea coupled mode is dominant by the surface  
329 heating. Mid-level heating that tends to cause baroclinic atmospheric response is not  
330 conducive to the unstable coupled mode while surface heating always benefits the  
331 instability. Figure 10a shows the variation of unstable growth rate with zonal  
332 wavelength and surface heating intensity. Here the mid-level heating is fixed and the  
333 surface heating is modified continuously by changing  $\gamma_2$ . It can be seen that  
334 corresponding to the fastest-growing mode, the stronger the surface heating is (the  
335 larger  $\gamma_2$  is), the more unstable the coupled mode becomes.

#### 336 **4.2 Role of transient eddy vorticity forcing with different vertical profiles**

337 Similarly, by setting  $\gamma_a = 0$  in equations (9) and (10), the diabatic heating is neglected.  
338 Transient eddy vorticity forcing becomes the only PV source of atmosphere. Here we  
339 also illustrate three cases with different vertical profiles of transient eddy vorticity  
340 forcing: when the vorticity forcing occurs only in lower troposphere ( $F_{eddy2} \neq$   
341  $0, F_{eddy1} = 0$ ), only in higher troposphere ( $F_{eddy2} = 0, F_{eddy1} \neq 0$ ), and in both layers  
342 ( $F_{eddy2}, F_{eddy1} \neq 0$ ).

343 In all the three cases, the oceanic Rossby wave mode can be unstable over the  
344 entire wavelength range (Fig. 8). However, in the lower-layer forcing case, the  
345 instability of the coupled mode is very weak. The growth rate of the most unstable mode  
346 is only  $0.0226$  ( $\text{yrs}^{-1}$ ), and the corresponding wavelength and period are  $8800\text{km}$   
347 and  $7.67$  yrs, respectively (Fig. 8b and e). While in the higher-layer forcing case, the

348 growth rate of the most unstable mode is increased evidently, corresponding to a longer  
349 wavelength 9900km and a longer period 8.17 yrs (Fig. 8a and d). Meanwhile, the spatial  
350 phase relationship between atmospheric streamfunction and SST anomaly (Fig. 9a and  
351 c) is closer to that of the standard case (Fig. 3a and b). When the transient eddy vorticity  
352 forcing at both layers are considered at the same time, the variation of growth rate is  
353 similar as that of the upper-layer forcing case, but the most unstable growth rate is  
354 increased slightly with zonal wavelength around 10200km and period of 8.34 yrs (Fig.  
355 8c and f). Therefore, the upper-layer transient eddy vorticity forcing plays a dominant  
356 role in producing unstable air-sea interaction mode.

357 However, it should be mentioned that in present study, the lower-layer transient  
358 eddy vorticity forcing is set to be 0.2 times of that of upper layer ( $\delta_2 = 0.2$ ) according  
359 to the observational analysis. If we assume the magnitudes of the forcing at both layers  
360 are equal ( $\delta_2 = 1.0$ ), which is equivalent to the setting in the atmospheric barotropic  
361 model (CYF2020), then the unstable growth rate is enhanced greatly no matter whether  
362 the higher-layer forcing is considered or not (as shown by the green lines in Fig. 8e and  
363 f). At this time, the contribution of individual lower-layer vorticity forcing on the  
364 unstable mode has overtook that of individual higher-layer forcing (Fig. 8d and e),  
365 suggesting that the lower-layer vorticity forcing stimulates instability more effectively.  
366 This can also be illustrated by Fig. 10b, in which the higher-layer forcing is fixed and  
367 the lower-layer forcing is changed continuously. With the increase of low-layer forcing,  
368 the unstable growth rate increases, and the fastest-growing mode moves to longer  
369 wavelength slightly. This phenomenon can also be explained by equations (7) and (8).  
370 According to the relationship between transient eddy vorticity forcing and SST  
371 anomalies, a cold SST anomaly will cause positive vorticity forcing in both layers. To  
372 the barotropic component of the atmosphere,  $F_{eddy2}$  has equal contribution with  
373  $F_{eddy1}$ . But to the baroclinic component,  $F_{eddy2}$  tends to decrease the baroclinic  
374 component by offsetting the contribution of  $F_{eddy1}$ . Hence the lower-layer

375 atmospheric response of geopotential low anomaly will become stronger and  
376 strengthens the cold SST anomaly more effectively through driving cyclonic oceanic  
377 flow.

378 Furthermore, although either diabatic heat forcing or transient eddy vorticity  
379 forcing can lead to unstable oceanic Rossby wave mode with similar equivalent  
380 barotropic structure, the latter has a much more contribution to the unstable growth rate  
381 (Fig.3b, 6f, 8f). It demonstrates that transient eddy dynamic feedback plays a more  
382 important role in unstable midlatitude ocean-atmosphere interaction. This conclusion is  
383 also consistent with that of previous theoretical study (Fang and Yang, 2016) and  
384 analytical model study with barotropic atmospheric model (CYF2020).

## 385 **5. Comparison with the results of coupled model with barotropic atmosphere**

386 In CYF2020, the atmosphere is assumed to be barotropic, and the diabatic heating only  
387 occurs at the top of boundary layer. Thus both the diabatic heat forcing that is  
388 proportional to the vertical gradient of diabatic heating and the transient eddy vorticity  
389 forcing are constant in the vertical direction. Nevertheless, as expressed by equations  
390 (7) and (8), in our present baroclinic atmospheric model, the surface diabatic heating  
391 only acts on lower-layer atmosphere whereas the mid-level heating impacts on both  
392 lower- and higher-layers but with opposite effect. Thus they both contribute to the  
393 baroclinic component and their contributions can offset each other to some extent.  
394 Moreover, if the transient eddy vorticity forcing is unchanged in vertical direction  
395 ( $F_{eddy1} = F_{eddy2}$ ), like in the barotropic model, it will only impact on the barotropic  
396 atmospheric component. Otherwise, the difference between the transient eddy vorticity  
397 forcing in the two layers will cause baroclinic atmospheric response.

398 Therefore the barotropic atmosphere model is equivalent to the barotropic  
399 component of atmosphere in our study if  $U$  and  $F_{eddy}$  are constant. Compared with  
400 the results of barotropic mode (orange line in Fig. 11a), the growth rate of the most

401 unstable oceanic Rossby wave (blue line in Fig. 11a) is reduced by 70%. One reason  
402 is due to the offset effect by the mid-level diabatic heating (Fig. 11b), and the other  
403 reason is due to the weakening of lower-layer transient eddy vorticity forcing (Fig. 11c).  
404 As mentioned in Section 3, because the vertical structures of atmospheric PV sources  
405 and basic flow are more realistic in the present baroclinic model, the associated period  
406 and spatial configuration patterns of the unstable coupled mode approach the  
407 observation much better.

## 408 **6. Contributions of other processes and factors**

### 409 **6.1 Relative roles of oceanic entrainment and advection processes**

410 In SST evolution equation (12), the oceanic processes determining SST change include  
411 horizontal advection, vertical entrainment and air-sea flux exchange, which represent  
412 the oceanic adjustment to the atmospheric forcing. The relative roles of different  
413 oceanic processes in destabilizing coupled oceanic Rossby wave mode are also  
414 examined below.

415 Since the air-sea flux exchange just can stimulate very weak damping mode  
416 (figure not shown), the main processes we emphasize here are entrainment and  
417 advection. Figure 12 shows the growth rate as a function of wavelength for the coupled  
418 oceanic Rossby wave mode for the cases of all oceanic processes, of entrainment only  
419 and of advection only, respectively. It can be found that both entrainment and advection  
420 have contributions to unstable coupled mode. When the wavelength is shorter than  
421 10000km, the total unstable growth is contributed primarily by advection, while over  
422 the wavelength range beyond 10000km, it is contributed jointly by advection and  
423 entrainment.

### 424 **6.2 Influence of coupling strength and basic zonal flows**

425 The unstable coupled mode may be influenced by two kinds of critical parameters, the  
426 coupling coefficients ( $\gamma_a$  and  $\gamma$ ) that determine the coupling strength between ocean

427 and atmosphere through thermal and dynamical processes, and the background zonal  
428 wind in the two atmospheric layers ( $U_1$  and  $U_2$ ). For our standard case, the values of  
429 these parameters are set as  $\gamma = 11.2s^{-2}m^2K^{-1}$ ,  $\gamma_a = 8 \times 10^{-7}s^{-1}$ ,  $U_1 = 17m/s$ ,  
430  $U_2 = 8m/s$ , respectively. The influence of air-sea coupling strength and basic zonal  
431 flows on unstable ocean-atmosphere interaction is then estimated by changing the  
432 relevant parameter alone.

433 Figure 13 shows the variation of growth rate of the most unstable Rossby wave  
434 mode with zonal wavelength versus dynamical coupling coefficient ( $\gamma$ ), thermal  
435 coupling coefficient ( $\gamma_a$ ), higher-layer basic zonal wind ( $U_1$ ), lower-layer basic zonal  
436 wind ( $U_2$ ), and vertical wind shear ( $\tilde{U} = U_1 - U_2$ ), respectively. The standard case is  
437 marked by “ $\times$ ” in the figure. It can be seen from Fig. 13a and b that the oceanic Rossby  
438 wave is always unstable within the present parameter field. With the increase of  
439 coupling strength, no matter dynamical coupling or thermal coupling, the instability of  
440 the coupled mode is enhanced. However, the influence of transient eddy dynamical  
441 feedback intensity is more prominent, because the enhancement amplitude is larger and  
442 the corresponding wavelength range is much wider. When the coupling is strengthened,  
443 the SST anomaly can force the atmosphere more strongly, especially through transient  
444 eddy vorticity forcing, thus the coupled mode becomes more unstable.

445 The intensity as well as vertical shear of the basic zonal wind is also a crucial  
446 factor that determining the vertical structure of atmospheric response to SST anomalies.  
447 When the basic zonal wind in higher layer is larger than that in lower layer ( $U_1 >$   
448  $8m/s$ ), the unstable growth rate decreases with the increase of  $U_1$  (Fig. 13c).  
449 Conversely, when the basic zonal wind in lower layer is less than that in higher layer  
450 ( $U_2 < 17m/s$ ), the unstable growth rate increases with the increase of  $U_2$  (Fig.13d).  
451 That is to say, the larger the vertical wind shear, the weaker the instability (Fig. 13e).  
452 When the basic zonal winds in both layers are equal, as in the barotropic model, the  
453 unstable growth rate reaches its maximum (Fig. 13e). That is because the vertical wind

454 shear tends to weaken the barotropic atmospheric response by vorticity advection and  
455 thus unbenefited to the unstable coupled mode.

## 456 **7. Conclusions and discussion**

457 Midlatitude ocean-atmosphere interaction is believed to be an important source of  
458 decadal to interdecadal climate variabilities. However, mechanism responsible for the  
459 midlatitude ocean-atmosphere interaction remains unclear for a long time primarily due  
460 to the lack of understanding on how midlatitude oceans affect the atmosphere.

461 Traditionally, people think the midlatitude SST impacts on the atmosphere mainly  
462 through diabatic heating, as in the tropics. But the pure thermal-driven circulation  
463 cannot explain the observed equivalent barotropic structure of decadal variabilities well.  
464 Meanwhile, the midlatitude atmosphere has strong baroclinicity, and the synoptic  
465 transient eddies accompanied with jet stream and storm track develop vigorously. The  
466 thermal and momentum transportation by transient eddies are also important forcing  
467 sources of midlatitude atmospheric circulation. Fang and Yang (2016) illustrated that  
468 SST anomaly could cause transient eddy forcing anomaly by changing the strength of  
469 oceanic front and thus the low-level atmospheric baroclinicity. The atmospheric  
470 response to the transient eddy vorticity forcing that dominates the total forcing, displays  
471 an equivalent barotropic structure, which further sustains the initial SST anomaly.  
472 Hence, transient eddy feedback in the middle latitudes, especially transient eddy  
473 dynamic feedback, has been recognized as another important approach for SST to affect  
474 the seasonal-mean atmosphere.

475 In our previous work (CYF2020), an analytical air-sea coupled model is  
476 established to investigate the contributions of TEDF to unstable ocean-atmosphere  
477 interaction in the middle latitudes. In the model, the atmosphere is assumed to be  
478 barotropic for zero-order approximation. In fact, since the midlatitude atmospheric  
479 stratification is stable, the diabatic heating is mainly confined to the lower troposphere,

480 and there is also a relatively weak heating center in the middle level of atmosphere.  
481 Meanwhile, though the transient eddy vorticity forcing has barotropic structure in the  
482 vertical direction, its large values primarily locates in middle to high troposphere. In  
483 order to resolve the realistic vertical structure of the atmospheric forcing better and  
484 further analyze their roles in midlatitude ocean-atmosphere interaction, in the present  
485 study, we extend the atmospheric component of the air-sea coupled model into a two-  
486 layer baroclinic model.

487 Both the atmospheric and oceanic components satisfy quasi-geostrophic dynamics  
488 and are governed by their QGPV equations on a midlatitude beta plane, respectively. A  
489 linearized mixed layer temperature equation is considered to describe the SST evolution.  
490 In the coupled model, the ocean is driven by the wind stress forcing of atmosphere and  
491 force the atmosphere in turn though diabatic heating and transient eddy vorticity forcing.  
492 The diabatic heating is specified at both the top of boundary layer and the interface of  
493 two layers, and the diabatic heat forcing in each atmospheric layer is proportional to  
494 the vertical gradient of diabatic heating. The transient eddy vorticity forcing in each  
495 layer is parameterized with the meridional second derivate of SST. Based on  
496 observation, the surface heating is set to be twice the mid-level heating, and the  
497 transient eddy vorticity forcing in lower layer is 0.2 times of that in higher layer for the  
498 standard case.

499 Midlatitude air-sea interaction produces two types of coupled modes, in which the  
500 oceanic Rossby wave mode that propagates westward destabilizes over the whole range  
501 of zonal wavelengths. The fastest-growing oceanic Rossby wave mode occurs at the  
502 wavelength around 9900km, with a period of nearly 8yrs. For this mode, the  
503 atmospheric streamfunction response in the two layers are both in phase with SST  
504 anomaly, with lows (highs) over cold (warm) water, and the oceanic streamfuction also  
505 shows a cyclonic (anticyclonic) circulation anomaly eastward slightly to the cold (warm)  
506 SST anomaly. Thus the unstable coupled mode exhibits an equivalent barotropic

507 structure similar to the observed decadal climate variability. Such configuration  
508 structure also suggests the following air-sea interaction processes, as illustrated in Fig.  
509 14. If there is an initial cold (warm) SST anomaly in the north (south), on the one hand,  
510 it induces strong surface cooling (warming) and weak mid-level cooling (warming),  
511 leading to positive (negative) diabatic heat forcing in both layers. On the other hand,  
512 the oceanic front is enhanced by the increase of meridional SST gradient, and so is the  
513 low-level atmospheric baroclinicity. The transient eddies become more active and  
514 transport more vorticity flux to the north, causing positive (negative) transient eddy  
515 vorticity forcing in the north (south) part for both layers. Therefore, through thermal  
516 and transient eddy dynamical forcing, the cold (warm) SST anomaly generates an in-  
517 phase atmospheric low (high) anomaly in each atmospheric layer. The surface low (high)  
518 pressure anomaly tends to sustain the cyclonic (anticyclonic) oceanic upper flow, and  
519 thus further develops the initial cold (warm) SST anomaly through oceanic advection  
520 and entrainment processes. Consequently, the amplitude of coupled oceanic Rossby  
521 wave grows due to the ocean-atmosphere interaction.

522         Relative roles of diabatic heating and transient eddy vorticity forcing with different  
523 vertical profiles in destabilizing the coupled oceanic Rossby wave are further analyzed.  
524 A SST anomaly can induce the same-sign surface and mid-level diabatic heating as well  
525 as opposite-sign transient eddy vorticity forcing in both layers of the atmosphere. The  
526 surface diabatic heating favors the barotropic component of atmosphere and restrains  
527 the baroclinic component. Hence it tends to cause barotropic atmospheric response and  
528 lead to unstable coupled mode. However, the mid-level heating always enhances the  
529 baroclinic component and thus decays the coupled mode by offsetting the effect of  
530 surface heating. The contribution of total diabatic heating on the coupled mode is  
531 dominated by surface heating. On the other hand, the transient eddy vorticity forcing of  
532 each layer can force barotropic atmospheric response and induce unstable coupled  
533 mode, while the lower-layer vorticity forcing can affect the unstable mode more

534 effectively by weakening the baroclinic response. However, in the standard case, the  
535 transient eddy vorticity forcing in lower layer is much smaller than that in higher layer,  
536 thus the higher-layer transient eddy vorticity forcing has more prominent contribution  
537 to the unstable growth rate. Although either diabatic heat forcing or transient eddy  
538 vorticity forcing can generate unstable coupled oceanic Rossby wave alone, the  
539 transient eddy dynamic feedback plays a much more important role.

540 Besides the SST-induced forcing on the atmosphere, the oceanic adjustment  
541 processes driven by the atmospheric circulation, which mainly include advection and  
542 entrainment, can also contribute to the unstable coupled mode. When SST is adjusted  
543 by advection process alone, the coupled oceanic Rossby wave with zonal wavelength  
544 shorter than 10000km tends to be unstable. When the entrainment process is considered  
545 alone, the unstable coupled mode moves to longer wavelength range ( $> 10000\text{km}$ ).  
546 Moreover, the influence of air-sea coupling strength and background zonal wind are  
547 also examined. When the coupling is strengthened, either dynamical coupling or  
548 thermal coupling, the instability of the coupled mode is enhanced. But the effect of  
549 dynamic coupling through transient eddy vorticity forcing is more significant. For the  
550 basic zonal wind, its barotropic part favors the growth of coupled mode, whereas its  
551 baroclinic part that determined by the vertical wind shear tends to decay the coupled  
552 mode.

553 Compared with the results derived from CYF2020, in which the atmospheric  
554 component is barotropic, the spatial configuration structure and period of the unstable  
555 coupled mode are more consistent with the observation. Nevertheless, it should be  
556 mentioned that there are actually three PV sources in the atmospheric QGPV equation:  
557 diabatic heat forcing, transient eddy heat forcing and transient eddy vorticity forcing  
558 (Fang and Yang, 2016). Transient eddy heat forcing is proportional to the vertical  
559 gradient of transient eddy heating ( $Q_{eddy}$ ) that represents the convergence/divergence  
560 of heat flux transported by transient eddies. Transient eddy heating that has the same

561 dimension of diabatic heating can be seen as an indirect heat source of the atmosphere,  
562 reflecting the transient eddy thermal forcing on the atmosphere. The magnitude of  
563 transient eddy heating is comparable with that of diabatic heating, and it mainly  
564 concentrates in the middle of troposphere (Fig. 2c in CYF2020). Hence in the barotropic  
565 model, it is neglected after vertical integration. In the present study, there is still on  
566 explicit performance of transient eddy heating in the coupled model. However, since it  
567 is equivalent to a mid-level heating, the case with equal diabatic heating at surface and  
568 middle level of atmosphere ( $\gamma_2 = 1$  in Fig. 10a) in this study can represent the  
569 condition in which the transient eddy heating is also considered in the coupled model.  
570 At this time, the growth rate of the most unstable coupled mode is decreased a little due  
571 to the enhancement of baroclinic response induced by transient eddy heating.

572 In addition, according to the form of plane wave solutions in our study, all the  
573 variables are required to be in phase in  $y$  direction. Thus the meridional phase shift  
574 as shown in Fig.5c and d cannot be obtained. If we use another form of plane wave  
575 solutions as  $(\psi_a, \psi_o, T_1)e^{i(kx+ly-\sigma t)}$ , there will not be closed spatial centers for the  
576 perturbation, but the meridional phase shift between SST and atmospheric  
577 streamfunction as well as oceanic streamfunction can be exhibited.

## 578 **Acknowledgements**

579 This study is jointly supported by the National Natural Science Foundation of China  
580 (Grant Nos. 41621005 and 41875086) and the National Key Basic Research and  
581 Development Program of China (Grant No. 2018YFC1505902). We are grateful for the  
582 support from the Jiangsu Collaborative Innovation Center for Climate Change.

583

584

585 **References**

- 586 Cayan DR (1992) Latent and sensible heat flux anomalies over the northern oceans:  
587 Driving the sea surface temperature. *J Phys Oceanogr* 22: 859-881.  
588 [https://doi.org/10.1175/1520-0485\(1992\)022<0859:LASHFA>2.0.CO;2](https://doi.org/10.1175/1520-0485(1992)022<0859:LASHFA>2.0.CO;2)
- 589 Chen L Chen, L., Fang, J. & Yang, X. Midlatitude unstable air-sea interaction with  
590 atmospheric transient eddy dynamical forcing in an analytical coupled  
591 model. *Clim Dyn* (2020). <https://doi.org/10.1007/s00382-020-05405-0>
- 592 Chu CJ, Yang XQ, Ren XJ, Zhou TJ (2013) Response of Northern Hemisphere storm  
593 tracks to Indian-western Pacific Ocean warming in atmospheric general  
594 circulation models. *Clim Dyn* 40(5–6):1057–1070.  
595 <https://doi.org/10.1007/s00382-013-1687-y>
- 596 Deser C, Blackman M (1993) Surface climate variations over the North Atlantic  
597 Ocean during winter: 1900–1989. *J Clim* 6:1743–1753.  
598 [https://doi.org/10.1175/1520-0442\(1993\)006<1743:SCVOTN>2.0.CO;2](https://doi.org/10.1175/1520-0442(1993)006<1743:SCVOTN>2.0.CO;2)
- 599 Enfield DB, Mestas-Nunez AM (1999) Multiscale variabilities in global sea surface  
600 temperatures and their relationships with tropospheric climate patterns. *J Clim*  
601 12:2719–2733. [https://doi.org/10.1175/1520-0442\(1999\)0122.0.CO;2](https://doi.org/10.1175/1520-0442(1999)0122.0.CO;2)
- 602 Fang J, Yang X-Q (2011) The relative roles of different physical processes in unstable  
603 midlatitude ocean-atmosphere interactions. *J Clim*, 24: 1542-1558.  
604 <https://doi.org/10.1175/2010JCLI3618.1>
- 605 Fang J, Yang X-Q (2016) Structure and dynamics of decadal anomalies in the  
606 wintertime midlatitude North Pacific ocean-atmosphere system. *Clim Dyn* 47:  
607 1989-2007. <https://doi.org/10.1007/s00382-015-2946-x>
- 608 Fang JB, Rong XY, Yang XQ (2006) Decadal-to-interdecadal response and  
609 adjustment of the North Pacific to prescribed surface forcing in an oceanic  
610 general circulation model. *Acta Oceanol Sin* 25(3):11–24.  
611 <https://doi.org/10.1016/j.marchem.2005.09.003>

612 Graham NE, Barnett TP, Wilde R, Ponater M, Schubert S (1994) On the roles of  
613 tropical and midlatitude SSTs in forcing interannual to interdecadal variability in  
614 the winter Northern Hemisphere circulation. *J Clim* 7:1416–1441.  
615 [https://doi.org/10.1175/1520-0442\(1994\)007<1416:OTROTA>2.0.CO;2](https://doi.org/10.1175/1520-0442(1994)007<1416:OTROTA>2.0.CO;2)

616 Gu D, Philander SGH (1997) Interdecadal climate fluctuations that depend on  
617 exchange between the tropics and extratropics. *Science* 275:805–807.  
618 <https://doi.org/10.1126/science.275.5301.805>

619 Hoskins BJ, and DJ Karoly (1981) The steady linear response of a spherical  
620 atmosphere to thermal and orographic forcing. *J. Atmos. Sci.*, 38, 1179–1196.  
621 [http://dx.doi.org/10.1175/1520-0469\(1981\)038<1179:TSLROA>2.0.CO;2](http://dx.doi.org/10.1175/1520-0469(1981)038<1179:TSLROA>2.0.CO;2)

622 Kushnir Y, Robinson WA, Bladé I, Hall NMJ, Peng S, Sutton R (2002) Atmospheric  
623 GCM response to extratropical SST anomalies: Synthesis and evaluation. *J Clim*  
624 15:2233–2256. [https://doi.org/10.1175/1520-](https://doi.org/10.1175/1520-0442(2002)015<2233:AGRTEA>2.0.CO;2)  
625 [0442\(2002\)015<2233:AGRTEA>2.0.CO;2](https://doi.org/10.1175/1520-0442(2002)015<2233:AGRTEA>2.0.CO;2)

626 Latif M, Barnett TP (1994) Causes of decadal climate variability over the North  
627 Pacific and North America. *Science* 266:634–637.  
628 <https://doi.org/10.1126/science.266.5185.634>

629 Latif M, Barnett TP (1996) Decadal climate variability over the North Pacific and  
630 North America: dynamics and predictability. *J Atmos Sci* 48: 2589–2631.  
631 [https://doi.org/10.1175/1520-0442\(1996\)009<2407:DCVOTN>2.0.CO;2](https://doi.org/10.1175/1520-0442(1996)009<2407:DCVOTN>2.0.CO;2)

632 Latif M, 1999: Dynamics of interdecadal variability in coupled ocean-atmosphere  
633 models. *Beyond El Niño: Decadal and Interdecadal Climate Variability*. A.  
634 Navarra, Ed., Springer Verlag, 213–250. [https://doi.org/10.1007/978-3-642-](https://doi.org/10.1007/978-3-642-58369-8_11)  
635 [58369-8\\_11](https://doi.org/10.1007/978-3-642-58369-8_11)

636 Lau NC, Holopainen EO (1984) Transient eddy forcing of the time-mean flow as  
637 identified by geopotential tendencies. *J Atmos Sci* 41: 313–328.  
638 [https://doi.org/10.1175/1520-0469\(1984\)041<0313:TEFOTT>2.0.CO;2](https://doi.org/10.1175/1520-0469(1984)041<0313:TEFOTT>2.0.CO;2)

639 Liu Z, Wu L (2004) Atmospheric response to North Pacific SST anomaly: the role of  
640 ocean–atmosphere coupling. *J Clim* 17:1859–1892. [https://doi.org/10.1175/1520-](https://doi.org/10.1175/1520-0442(2004)017<1859:ARTNPS>2.0.CO;2)  
641 [0442\(2004\)017<1859:ARTNPS>2.0.CO;2](https://doi.org/10.1175/1520-0442(2004)017<1859:ARTNPS>2.0.CO;2)

642 Liu CJ, Ren XJ, Yang XQ (2014) Mean flow-storm track relationship and Rossby  
643 wave breaking in two types of El-Niño. *Adv Atmos Sci* 31(1):197–210.  
644 <https://doi.org/10.1007/s00376-013-2297-7>

645 Mantua NJ, Hare SR, Zhang Y, Wallace JM, Francis RC (1997) A Pacific  
646 interdecadal climate oscillation with impacts on salmon production. *Bull Am*  
647 *Meteorol Soc* **78**, 1069-1079. [https://doi.org/10.1175/1520-](https://doi.org/10.1175/1520-0477(1997)078<1069:APICOW>2.0.CO;2)  
648 [0477\(1997\)078<1069:APICOW>2.0.CO;2](https://doi.org/10.1175/1520-0477(1997)078<1069:APICOW>2.0.CO;2)

649 Minobe S (1997) A 50-70 year climatic oscillation over the North Pacific and North  
650 America. *Geophys Res Lett* 24: 683-686. <https://doi.org/10.1029/97GL00504>

651 Nakamura H, Sampe T, Tanimoto Y, Shimpo A (2004) Observed associations among  
652 storm tracks, jet streams and midlatitude oceanic fronts. *Earth’s climate: the*  
653 *ocean–atmosphere interaction*. *Geophys. Monogr.*, vol 147. American  
654 Geophysical Union, pp 329–345. <https://doi.org/10.1029/147GM18>

655 Namias J, Cayan DR (1981) Large-scale air–sea interactions and short period climate  
656 fluctuations. *Science* 214:869–876. [https://doi.org/ 10.1126/science.214.4523.869](https://doi.org/10.1126/science.214.4523.869)

657 Neelin JD, Weng W (1999) Analytical prototypes for ocean-atmosphere interaction at  
658 midlatitudes. Part I: Coupled feedbacks as a sea surface temperature dependent  
659 stochastic process. *J Clim* 12: 697-721. [https://doi.org/10.1002/1175/1520-](https://doi.org/10.1002/1175/1520-0442(1999)012<0697:APFOAI>2.0.CO;2)  
660 [0442\(1999\)012<0697:APFOAI>2.0.CO;2](https://doi.org/10.1002/1175/1520-0442(1999)012<0697:APFOAI>2.0.CO;2)

661 Nie Y, Zhang Y, Yang XQ, Chen G (2013) Baroclinic anomalies associated with the  
662 Southern Hemisphere annular mode: roles of synoptic and low-frequency eddies.  
663 *Geophys Res Lett* 40:2361–2366. <https://doi.org/10.1002/grl.50396>

664 Nie Y, Zhang Y, Chen G, Yang XQ, Alex Burrows D (2014) Quantifying barotropic  
665 and baroclinic eddy feedbacks in the persistence of the Southern Annular Mode.  
666 Geophys Res Lett 41:8636–8644.<https://doi.org/10.1002/2014GL062210>

667 Pedlosky J (1970) Finite-amplitude baroclinic waves. J Atmos Sci 27: 15-30.  
668 [https://doi.org/10.1175/1520-0469\(1970\)027<0015:FABW>2.0.CO;2](https://doi.org/10.1175/1520-0469(1970)027<0015:FABW>2.0.CO;2)

669 Qiu B, Schneider N, Chen S (2007) Coupled decadal variability in the North Pacific:  
670 an observationally constrained idealized model. J Clim 20:3602–3620.  
671 <https://doi.org/10.1175/JCLI4190.1>

672 Qiu S, FANG J-B, YANG X-Q. Mid-Latitude Atmospheric Responses to Heat and  
673 Vorticity Using a Linear Baroclinic Model. J Meteor Sci, 2014, 34: 149-161.  
674 <https://doi.org/10.3969/2013jms.0060>

675 Ren XJ, Yang XQ, Chu CJ (2010) Seasonal variations of the synoptic- scale transient  
676 eddy activity and polar-front jet over east Asia. J Clim 23(12):3222–  
677 3233.<https://doi.org/10.1175/2009JCLI3225.1>

678 Robertson AW (1996): Interdecadal variability over the North Pacific in a multi-  
679 century climate simulation. Clim Dyn 12: 227–241.  
680 <https://doi.org/10.1007/BF00219498>

681 Saravanan R, McWilliams JC (1997) Stochasticity and spatial resonance in  
682 interdecadal climate fluctuations. J Clim 10: 2299–2320.  
683 [https://doi.org/10.1175/1520-0442\(1997\)0102.0.CO;2](https://doi.org/10.1175/1520-0442(1997)0102.0.CO;2)

684 Saravanan R, McWilliams JC (1998) Advective ocean-atmosphere interaction: An  
685 analytical stochastic model with implications for decadal variability. J Clim 11:  
686 165-188. [https://doi.org/10.1175/1520-  
687 0442\(1998\)011<0165:AOAIAA>2.0.CO;2](https://doi.org/10.1175/1520-0442(1998)011<0165:AOAIAA>2.0.CO;2)

688 Shutts G (1987) Some comments on the concept of thermal forcing. Q J R Meteorol  
689 Soc 113: 1387-1394. <https://doi.org/10.1002/qj.49711347817>

690 Small RJ, deSzoeko SP, Xie SP, O'Neill L, Seo H, Song Q, Cornillon P, Spall M,  
691 Minobe S (2008) Air–sea interaction over ocean fronts and eddies. Dyn Atmos

692 Oceans 45:274–319. <https://doi.org/10.1016/j.dynatmoce.2008.01.001>

693 Tao L, Yang X-Q, Fang J, Sun X (2020) PDO-related wintertime atmospheric  
694 anomalies over the midlatitude North Pacific: Local versus remote SST forcing. *J*  
695 *Clim*. <https://doi.org/10.1175/JCLI-D-19-0143.1>

696 Trenberth KE (1990) Recent observed interdecadal climate changes in the Northern  
697 Hemisphere. *Bull Am Meteorol Soc* 71:988–993. [https://doi.org/10.1175/1520-0477\(1990\)071<0988:ROICCI>2.0.CO;2](https://doi.org/10.1175/1520-0477(1990)071<0988:ROICCI>2.0.CO;2)

699 Wang L, Yang X-Q Yang, Yang D, Xie Q, Fang J, Sun X (2017) Two typical modes  
700 in the variabilities of wintertime North Pacific basin-scale oceanic fronts and  
701 associated atmospheric eddy-driven jet. *Atmospheric Science Letters*, 18: 373-  
702 380, doi: 10.1002/asl.766.

703 Wang L, Hu H, Yang X-Q (2019) The atmospheric responses to the intensity  
704 variability of subtropical front in the wintertime North Pacific. *Clim Dyn* 52:  
705 5623-5639. <https://doi.org/10.1007/s00382-018-4468-9>

706 Xiang Y, Yang XQ (2012) The effect of transient eddy on interannual meridional  
707 displacement of summer east Asian subtropical jet. *Adv Atmos Sci* 29(3):484–  
708 492. <https://doi.org/10.1007/s00376-011-1113-5>

709 Zhang R, Fang J, and Yang X-Q (2020) What kinds of atmospheric anomalies drive  
710 wintertime North Pacific basin-scale subtropical oceanic front intensity  
711 variation? *Journal of Climate*, 33 (16): 7011-7026, doi: 10.1175/JCLI-D-19-  
712 0973.1.

713 Zhang Y, Yang XQ, Nie Y, Chen G (2012) Annular-mode-like variation in a multi-  
714 layer QG model. *J Atmos Sci* 69(10):2940–2958. <https://doi.org/10.1175/JAS-D-11-0214.1>

716 Zhong YF, Liu Z, Jacob R (2008) Origin of Pacific multi-decadal variability in  
717 Community Climate System Model version (CCSM3): a combined statistical and

718 dynamical assessment. J Clim 21:114–133.  
719 <https://doi.org/10.1175/2007JCLI1730.1>

720 Zorita E, and Frankignoul C(1997) Modes of North Atlantic decadal variability in the  
721 ECHAM1/LSG coupled ocean–atmosphere general circulation model. J Clim 10:  
722 183–200. [https://doi.org/10.1175/1520-](https://doi.org/10.1175/1520-0442(1997)010<0183:MONADV>2.0.CO;2)  
723 [0442\(1997\)010<0183:MONADV>2.0.CO;2](https://doi.org/10.1175/1520-0442(1997)010<0183:MONADV>2.0.CO;2)

724 Zhu YM, Yang XQ (2003) Joint propagating patterns of SST and SLP anomalies in  
725 the North Pacific on bidecadal and pentadecadal timescales. Adv Atmos Sci  
726 20(5):694–710. <https://doi.org/10.1007/BF02915396>

727 Zhu YM, Yang XQ, Xie Q, Yu YQ et al (2008b) Decadal variability in the North  
728 Pacific as simulated by FGOALS-g fast coupled climate model. Chin J Geophys  
729 51(1):58–69. <https://doi.org/10.1002/cjg2.1194>

730  
731

**Table 1.** Standard values of parameters used in the coupled air-sea model

Symbol	Parameter	Value
$f$	Coriolis parameter	$1 \times 10^{-4} s^{-1}$
$\beta$	Meridional gradient of $f$	$1.8 \times 10^{-11} (ms)^{-1}$
$\alpha$	Wind stress coupling constant	$3 \times 10^{-8} s^{-1}$
$L_o$	Oceanic Rossby radius of deformation	45km
$L_a$	Atmospheric Rossby radius of deformation	660km
$l$	Meridional wavenumber	$2\pi/(6400km)$
$T_r$	Reference temperature of deep layer	283K
$\bar{T}_1^c$	Mean sea surface temperature	293K
$N_a^2$	Square of the atmospheric Brunt–Väisälä buoyancy frequency	$4.356 \times 10^{-5} s^{-2}$
$C_p$	Oceanic specific heat at constant pressure	$4000 Jkg^{-1} K^{-1}$
$b$	Buoyancy of thermocline	$2.5 \times 10^{-2} N$
$U_1$	Mean zonal wind for atmospheric layer 1	$17ms^{-1}$
$U_2$	Mean zonal wind for atmospheric layer 2	$8ms^{-1}$
$c_4$	Mean oceanic meridional temperature gradient	$3 \times 10^{-6} K m^{-1}$
$r_s$	Rayleigh damping coefficient	$1.3 \times 10^{-7} s^{-1}$
$r$	Diffusive coefficient	1/(5day)
$z(h)$	Height of atmospheric boundary layer	1200m
$H_a$	Depth of free troposphere	10km
$H_1$	Mixed layer depth	100m
$H$	Mean ocean upper-layer depth	500m
$H_2$	Thermocline layer mean depth	400m
$\Delta h_e$	Entrainment layer depth	40m
$\theta_{a0}$	Typical atmospheric potential temperature	290K
$\gamma_0$	Oceanic air-sea flux parameter	$5 \times 10^{-8} s^{-1}$
$\gamma_a$	Coupling coefficient for diabatic heating forcing	$8 \times 10^{-7} s^{-1}$
$\gamma$	Coupling coefficients for transient eddy vorticity forcing	$11.2s^{-2} m^2 K^{-1}$
$\gamma_2$	Ratio of surface diabatic heating to mid-level heating	2
$\delta_2$	Ratio of transient eddy vorticity forcing in lower layer to that in higher layer	0.2

733 **Figure captions**

734 **Figure 1.** Schematic diagram of vertical structure of the analytical midlatitude  
735 coupled ocean–atmosphere model and corresponding variables.

736 **Figure 2.** Latitude-altitude sections of regressed wintertime (DJF) anomalies  
737 (shading) upon the standardized PDO index during 1960-2010 for (a) geopotential  
738 height (units:  $m$ ), (b) diabatic heating (units:  $K/day$ ), and (c) transient eddy  
739 vorticity forcing (units:  $10^{-10}s^{-2}$ ), averaged between  $150^{\circ}E$  and  $150^{\circ}W$ , in which  
740 the black contours in (b, c, d) represent their corresponding climatologies, and the  
741 dots indicate the regions passing the student  $t$ -test at 95% significant level. A  
742 corresponding meridional distribution of regressed sea surface temperature anomalies  
743 (units:  $K$ ) is shown in the lower panel of (a). This figure is quoted from CYF2020 .

744 **Figure 3.** Climatological distributions of wintertime (a) SST (units:  $K$ ), (b) 2m-air  
745 temperature (units:  $K$ ), (c) negative meridional gradient of SST (units:  $10^{-5}K \cdot$   
746  $m^{-1}$ ), (d) negative meridional gradient of 2m-air temperature (units:  $10^{-5}K \cdot m^{-1}$ ),  
747 (e) Eady growth rate at 850 hPa (units:  $day^{-1}$ ), and (f) zonal wind (units:  $m/s$ ) at  
748 300 hPa for 1960-2010.

749 **Figure 4.** Spatial phase relationships between the SST anomaly (shaded) and (a) the  
750 upper-layer atmospheric streamfunction anomaly, (b) the lower-layer atmospheric  
751 streamfunction anomaly and (c) the upper-oceanic streamfunction anomaly (contours)  
752 for the fastest-growing coupled oceanic Rossby mode, given a fixed meridional  
753 wavelength at 6400 km. The largest amplitude of the SST anomaly is specified as 2K.

754 **Figure 5.** Spatial distributions of regressed wintertime anomalies (shading) upon the  
755 standardized PDO index during 1960-2010 for (a) SST (units:  $K$ ), (b) 2m-air  
756 temperature (units:  $K$ ), (c) negative meridional gradient (units:  $10^{-5}K \cdot m^{-1}$ ) of  
757 SST, (d) negative meridional gradient (units:  $10^{-5}K \cdot m^{-1}$ ) of 2m-air temperature,  
758 (e) Eady growth rate at 850 hPa (units:  $day^{-1}$ ), and (f) zonal wind (units:  $m/s$ ) at

759 300 hPa. The dots indicate the regions passing the student  $t$ -test at 95% significant  
760 level.

761 **Figure 6.** Frequency (a, c, e) and growth rate (b, d, f) of the coupled oceanic Rossby  
762 wave mode as a function of zonal wavelength corresponding to the surface diabatic  
763 heating only case (a, b), the mid-level heating only case(c, d) and the both surface and  
764 mid-level heating case (e, f), respectively. Red lines in (a, c, e) denote the frequency  
765 of free oceanic Rossby wave.

766 **Figure 7.** As in Fig. 4, but derived with (left) the surface diabatic heating alone and  
767 (right) the mid-level diabatic heating alone.

768 **Figure 8.** Frequency (a, b, c) and growth rate (blue lines in d, e, f) of the coupled  
769 oceanic Rossby wave mode as a function of zonal wavelength corresponding to cases  
770 when the transient eddy vorticity forcing occurs in lower layer only (a, d), in higher  
771 layer only (b, e), and in both layers (c, f), respectively. Green lines in (e, f) indicate  
772 the associated growth rate when the transient eddy vorticity forcing in lower layer is  
773 increased to be equal to that in higher layer. Red lines in (a, c, e) denote the frequency  
774 of free oceanic Rossby wave.

775 **Figure 9.** Spatial phase relationships among characteristic SST (blue line)  
776 atmospheric streamfunction (green lines) and upper-oceanic streamfunction (purple  
777 lines) anomalies in (a)  $X$  direction and (b)  $Y$  direction, respectively, for the fastest  
778 growing coupled oceanic Rossby mode. As a comparison, the observed wintertime  
779 SST anomalies (shading, units: degree in  $K$ ) together with vertical integration of  
780 atmospheric streamfunction anomalies (contours, units:  $10^{-4}m^2/s$ ), and SST  
781 anomalies together with upper-oceanic streamfunction anomalies (contours, units:  
782  $10^{-4}m^2/s$ ), regressed on the standardized PDO index, are shown in (c) and (d),  
783 respectively.

784 **Figure 10.** Unstable growth rate of coupled oceanic Rossby wave mode as a function  
785 of zonal wavelength versus (a) the ratio of surface heating to mid-level heating ( $\gamma_2$ ,  
786 here the mid-level heating is fixed and the surface heating is enhanced with the  
787 increase of  $\gamma_2$ ), and (b) the ratio of lower-layer transient eddy vorticity forcing to  
788 higher-layer vorticity forcing ( $\delta_2$ , here the higher-layer vorticity forcing is fixed and  
789 the lower-layer vorticity forcing is enhanced with the increase of  $\delta_2$ ), respectively.

790 **Figure 11.** Comparison of the growth rate of the coupled oceanic Rossby wave mode  
791 derived in our study with that derived in CYF2020 when (a) both diabatic heating and  
792 transient eddy vorticity forcing are considered simultaneously, (b) the diabatic heating  
793 is considered only and (c) the transient eddy vorticity forcing is considered only.

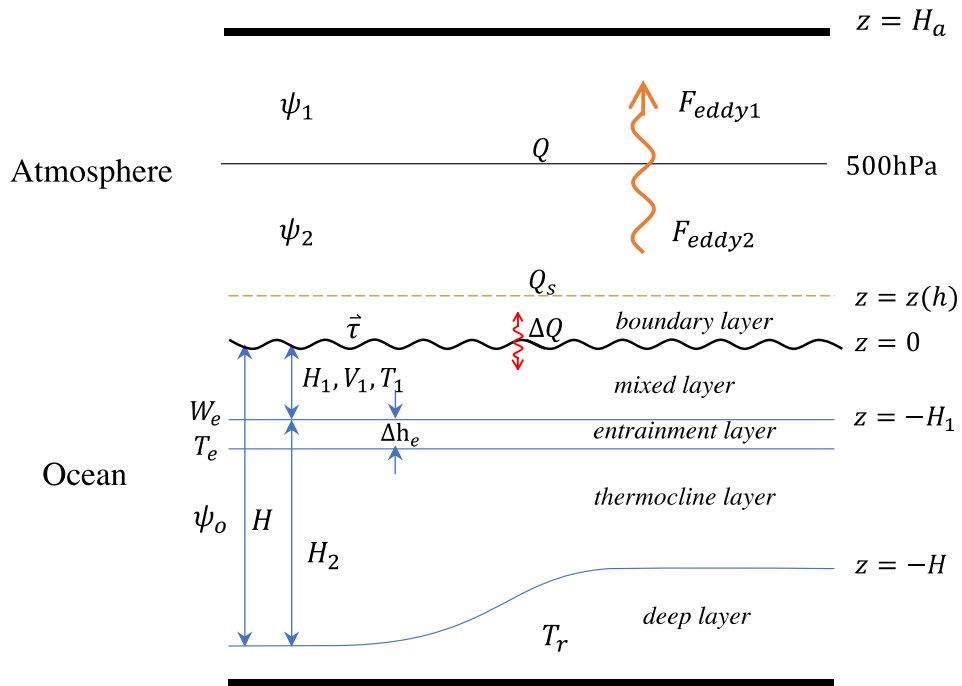
794 **Figure 12.** Growth rate as a function of wavelength for the coupled oceanic Rossby  
795 wave mode with (a) full oceanic processes in SST evolution equation, (b)  
796 entrainment- process only, and (c) advection process only. Note that (a) is the same as  
797 Fig. 3b.

798 **Figure 13.** Unstable growth rate of coupled oceanic Rossby wave mode as a function  
799 of zonal wavelength versus (a) dynamical coupling coefficient ( $\gamma$ ), (b) thermal  
800 coupling coefficient ( $\gamma_a$ ), (c) the higher-layer background zonal wind ( $U_1$ ), (d) the  
801 lower-layer background zonal wind ( $U_2$ ) and (e) the vertical wind shear ( $U_1 - U_2$ ),  
802 respectively.

803 **Figure 14.** Schematic diagram of the phase relationships among atmospheric and  
804 oceanic variables for the most unstable coupled oceanic Rossby wave mode in the  
805 midlatitudes.

806

807



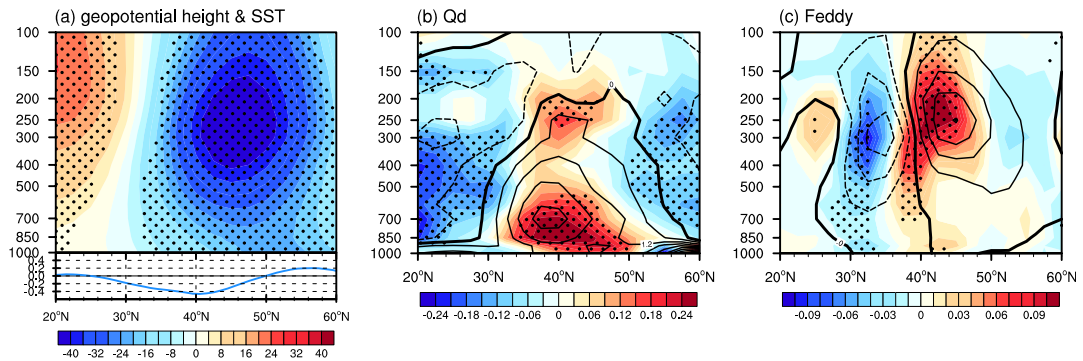
808

809 **Figure 1.** Schematic diagram of vertical structure of the analytical midlatitude

810 coupled ocean-atmosphere model and corresponding variables.

811

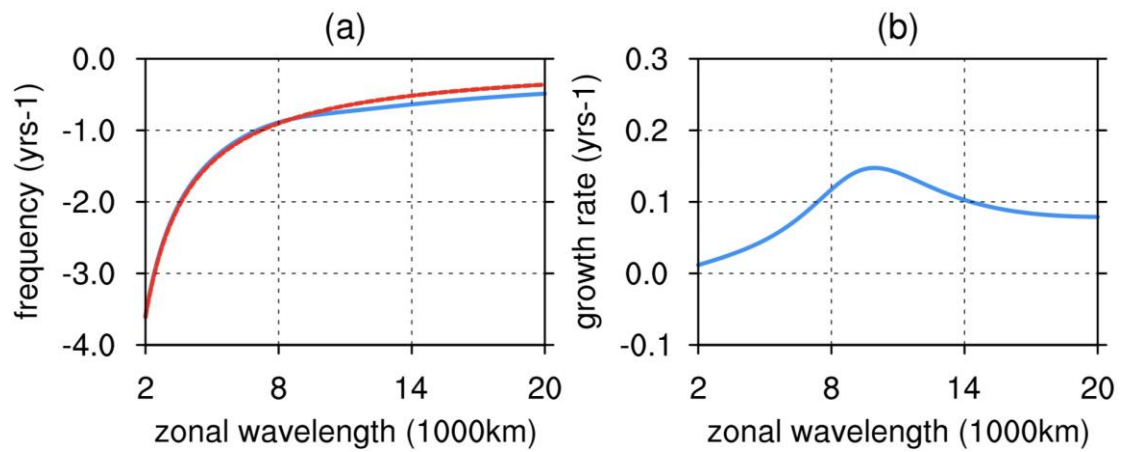
812



813

814 **Figure 2.** Latitude-altitude sections of regressed wintertime (DJF) anomalies  
815 (shading) upon the standardized PDO index during 1960-2010 for (a) geopotential  
816 height (units:  $m$ ), (b) diabatic heating (units:  $K/day$ ), and (c) transient eddy  
817 vorticity forcing (units:  $10^{-10}s^{-2}$ ), averaged between  $150^{\circ}E$  and  $150^{\circ}W$ , in which  
818 the black contours in (b, c, d) represent their corresponding climatologies, and the  
819 dots indicate the regions passing the student  $t$ -test at 95% significant level. A  
820 corresponding meridional distribution of regressed sea surface temperature anomalies  
821 (units:  $K$ ) is shown in the lower panel of (a). This figure is quoted from CYF2020.

822



823

824

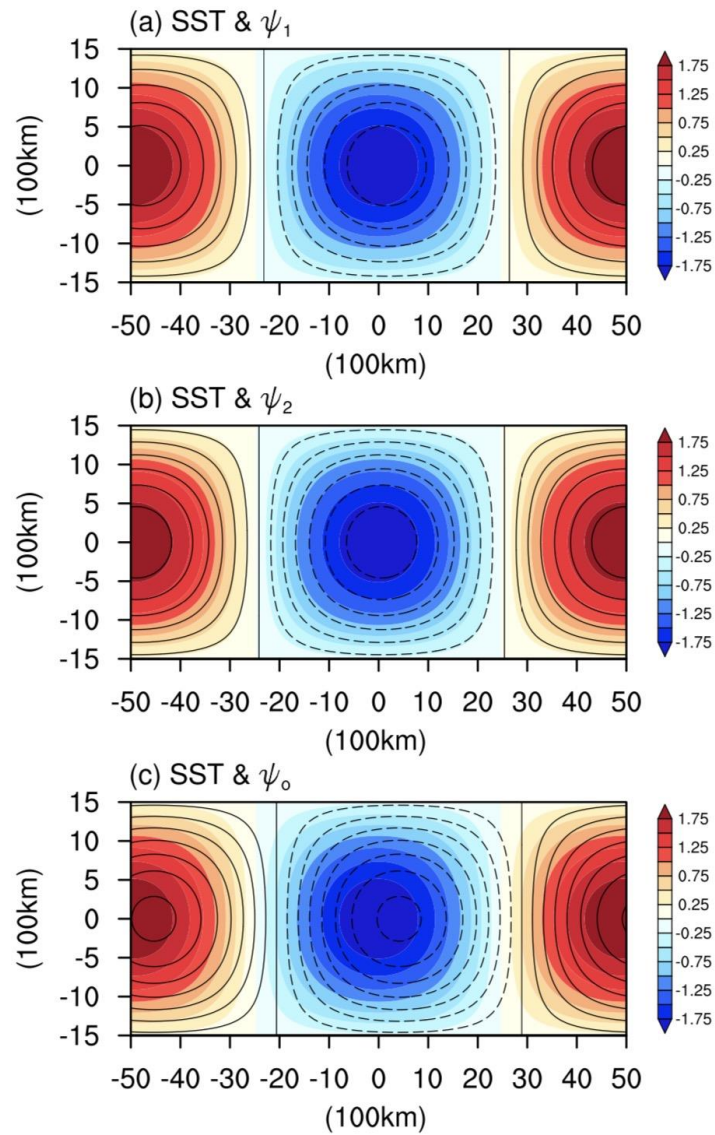
825

826 **Figure 3.** (a) Frequency and (b) growth rate of the coupled oceanic Rossby wave

827 mode as a function of zonal wavelength. The red line in (a) denotes the frequency of

828 free oceanic Rossby wave.

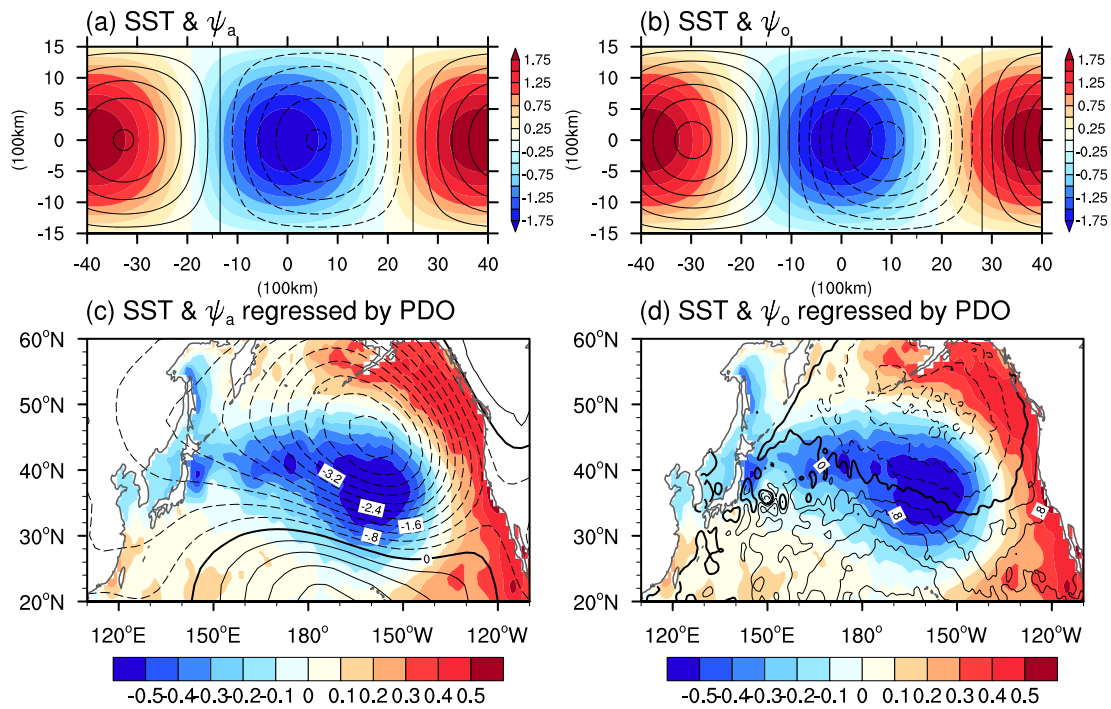
829



831

832 **Figure 4.** Spatial phase relationships between the SST anomaly (shaded) and (a) the  
 833 upper-layer atmospheric streamfunction anomaly, (b) the lower-layer atmospheric  
 834 streamfunction anomaly and (c) the upper-oceanic streamfunction anomaly  
 835 (contours) for the fastest-growing coupled oceanic Rossby mode, given a fixed  
 836 meridional wavelength at 6400 km. The largest amplitude of the SST anomaly is  
 837 specified as 2K.

838



839

840 **Figure 5.** Spatial phase relationships between characteristic SST anomaly (shaded)  
 841 and (a) barotropic atmospheric streamfunction anomaly and (b) upper-oceanic  
 842 streamfunction anomaly (contours) for the fastest-growing coupled oceanic Rossby  
 843 mode in CYF2020. The observed wintertime SST anomalies (shaded, units: degree in  
 844 *K*) together with (c) vertical integration of atmospheric streamfunction anomalies  
 845 (contours, units:  $10^{-4}m^2/s$ ), and (d) upper-oceanic streamfunction anomalies  
 846 (contours, units:  $10^{-4}m^2/s$ ), regressed on the standardized PDO index, are shown in  
 847 (c) and (d), respectively. This figure is quoted form CYF2020.

848

849

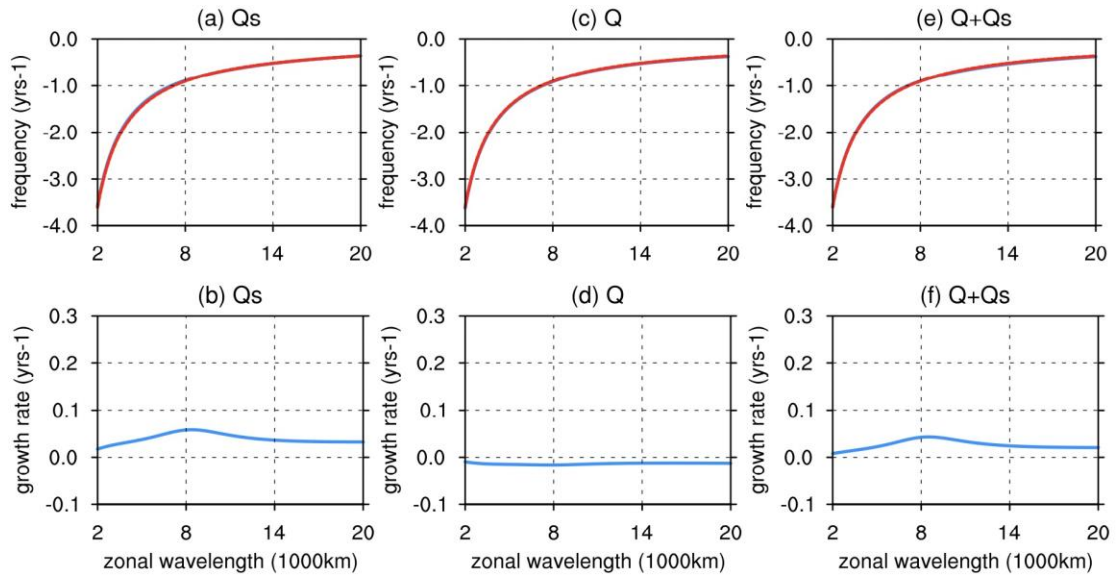
850

851

852

853

854

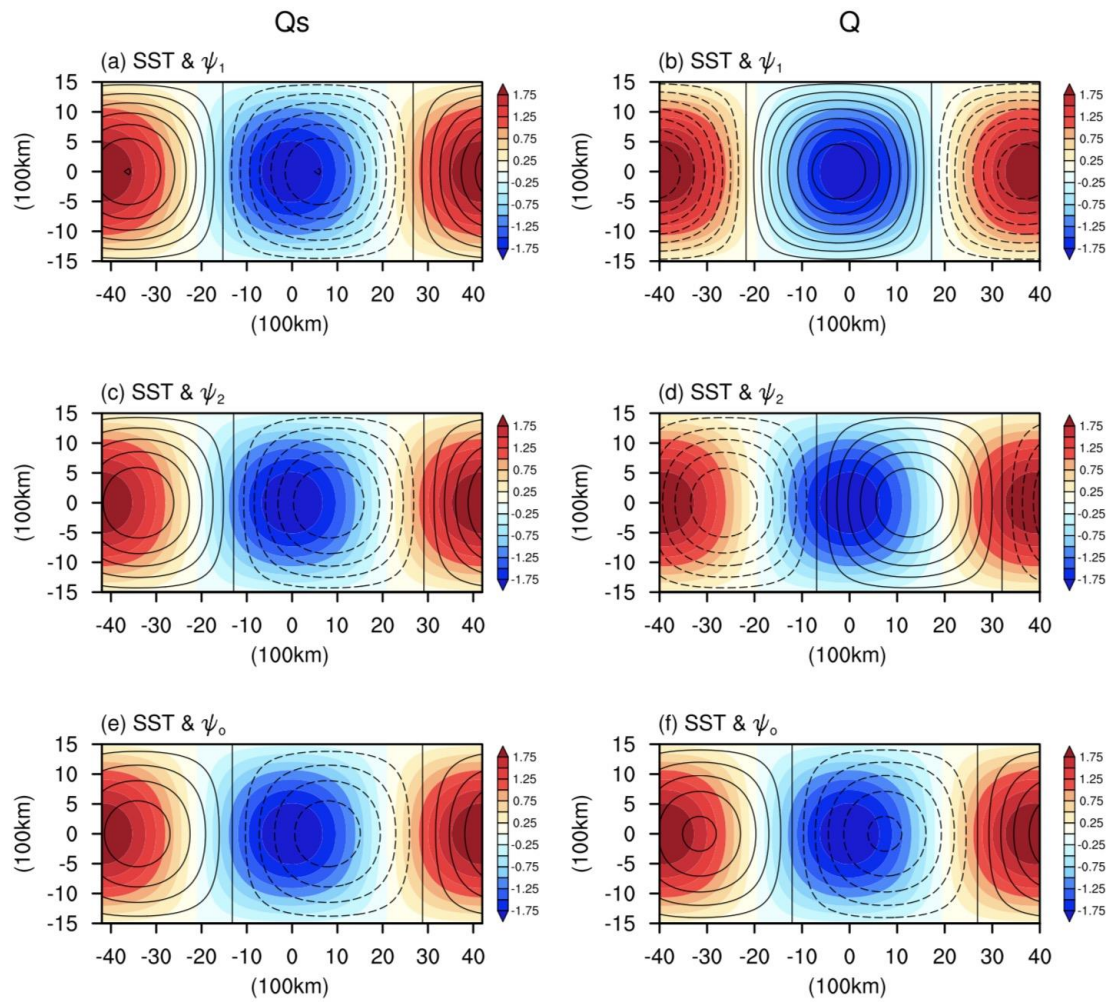


855

856 **Figure 6.** Frequency (a, c, e) and growth rate (b, d, f) of the coupled oceanic Rossby  
857 wave mode as a function of zonal wavelength corresponding to the surface diabatic  
858 heating only case (a, b), the mid-level heating only case(c, d) and the both surface and  
859 mid-level heating case (e, f), respectively. Red lines in (a, c, e) denote the frequency  
860 of free oceanic Rossby wave.

861

862



863

864

865 **Figure 7.** As in Fig. 4, but derived with (left) the surface diabatic heating alone and

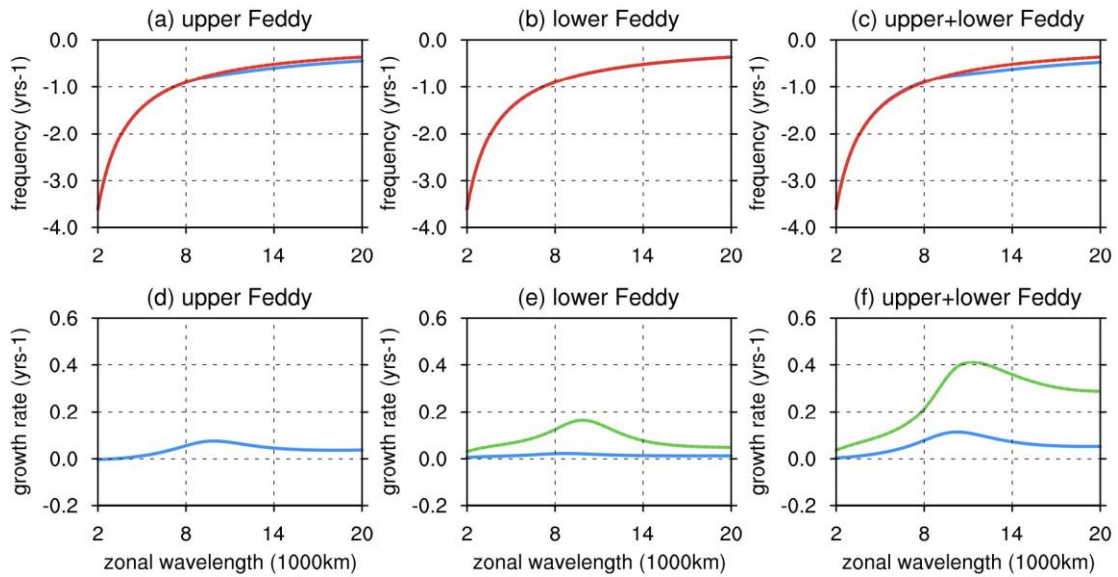
866 (right) the mid-level diabatic heating alone.

867

868

869

870

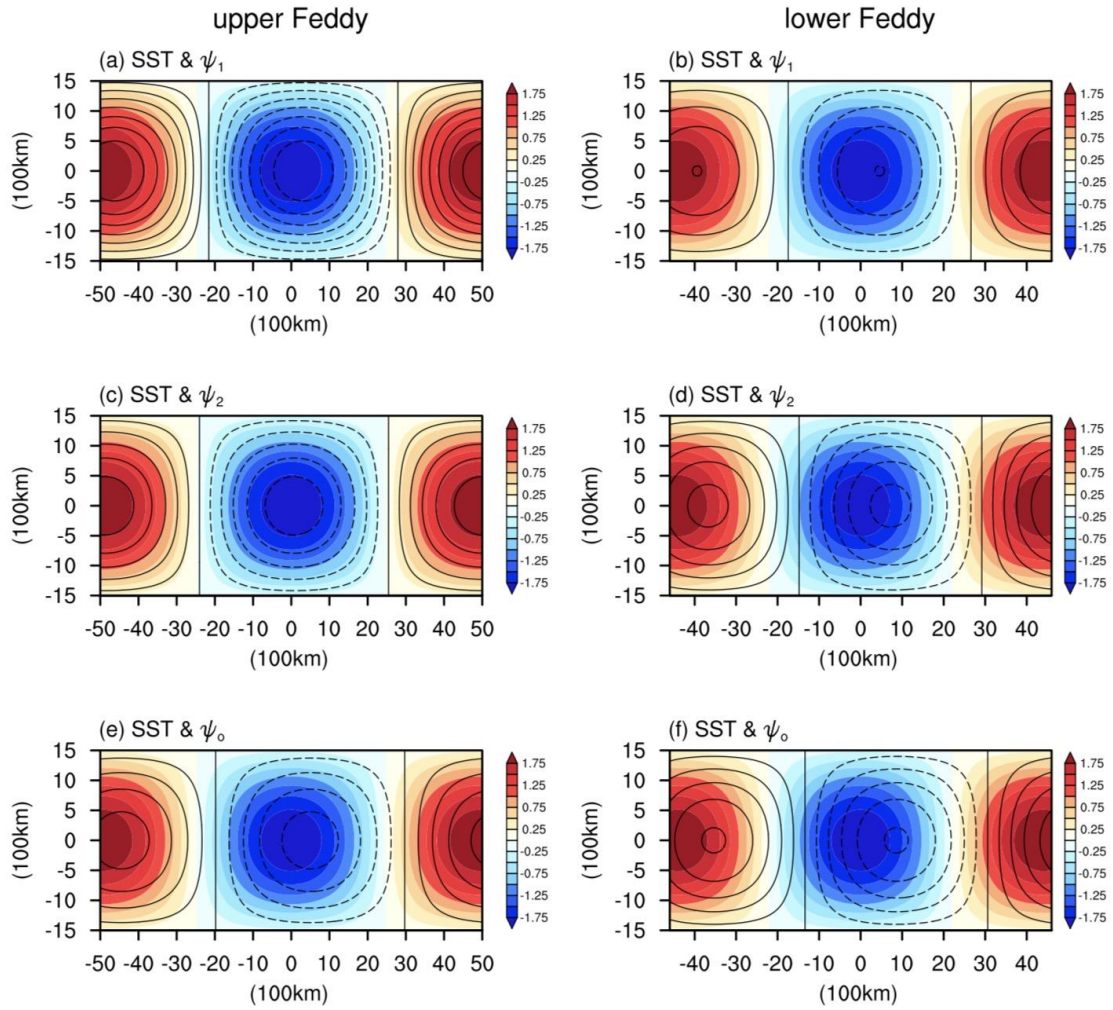


871

872

873 **Figure 8.** Frequency (a, b, c) and growth rate (blue lines in d, e, f) of the coupled  
874 oceanic Rossby wave mode as a function of zonal wavelength corresponding to cases  
875 when the transient eddy vorticity forcing occurs in lower layer only (a, d), in higher  
876 layer only (b, e), and in both layers (c, f), respectively. Green lines in (e, f) indicate  
877 the associated growth rate when the transient eddy vorticity forcing in lower layer is  
878 increased to be equal to that in higher layer. Red lines in (a, c, e) denote the frequency  
879 of free oceanic Rossby wave.

880

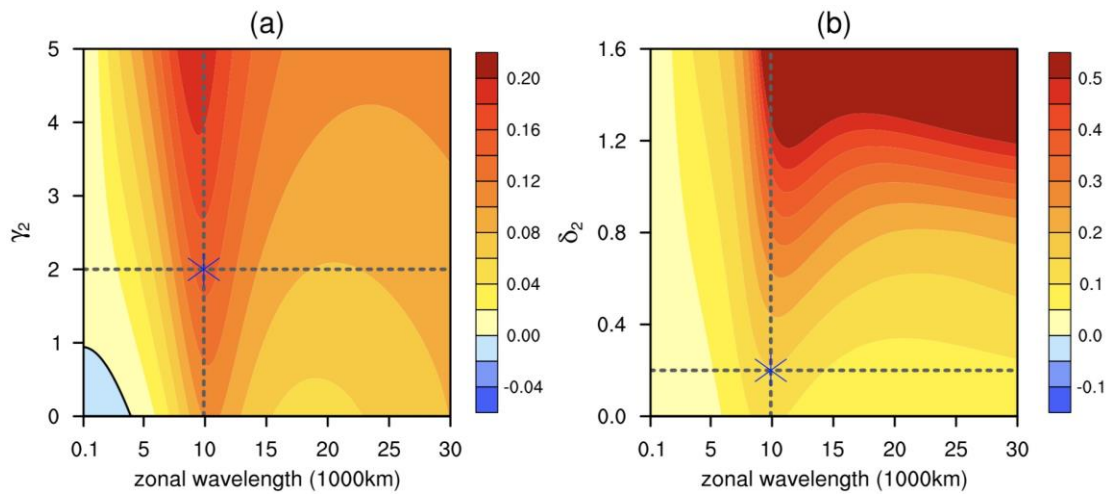


881

882 **Figure 9.** As in Fig. 4, but derived with (left) the lower-layer transient eddy vorticity  
 883 forcing alone and (right) the higher-layer transient eddy vorticity forcing alone.

884

885

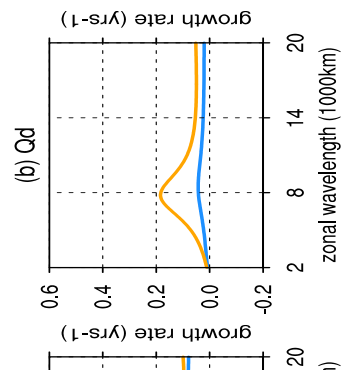


886

887 **Figure 10.** Unstable growth rate of coupled oceanic Rossby wave mode as a function  
888 of zonal wavelength versus (a) the ratio of surface heating to mid-level heating ( $\gamma_2$ ,  
889 here the mid-level heating is fixed and the surface heating is enhanced with the  
890 increase of  $\gamma_2$ ), and (b) the ratio of lower-layer transient eddy vorticity forcing to  
891 higher-layer vorticity forcing ( $\delta_2$ , here the higher-layer vorticity forcing is fixed and  
892 the lower-layer vorticity forcing is enhanced with the increase of  $\delta_2$ ), respectively.

893

894

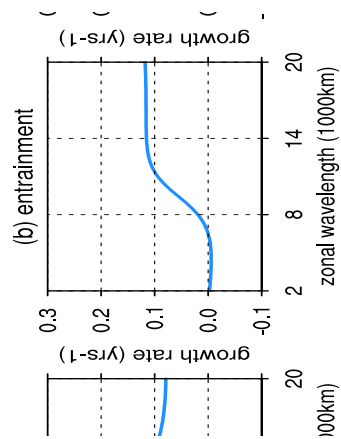


895

896 **Figure 11.** Comparison of the growth rate of the coupled oceanic Rossby wave mode  
897 derived in our study with that derived in CYF2020 when (a) both diabatic heating and  
898 transient eddy vorticity forcing are considered simultaneously, (b) the diabatic heating  
899 is considered only and (c) the transient eddy vorticity forcing is considered only.

900

901

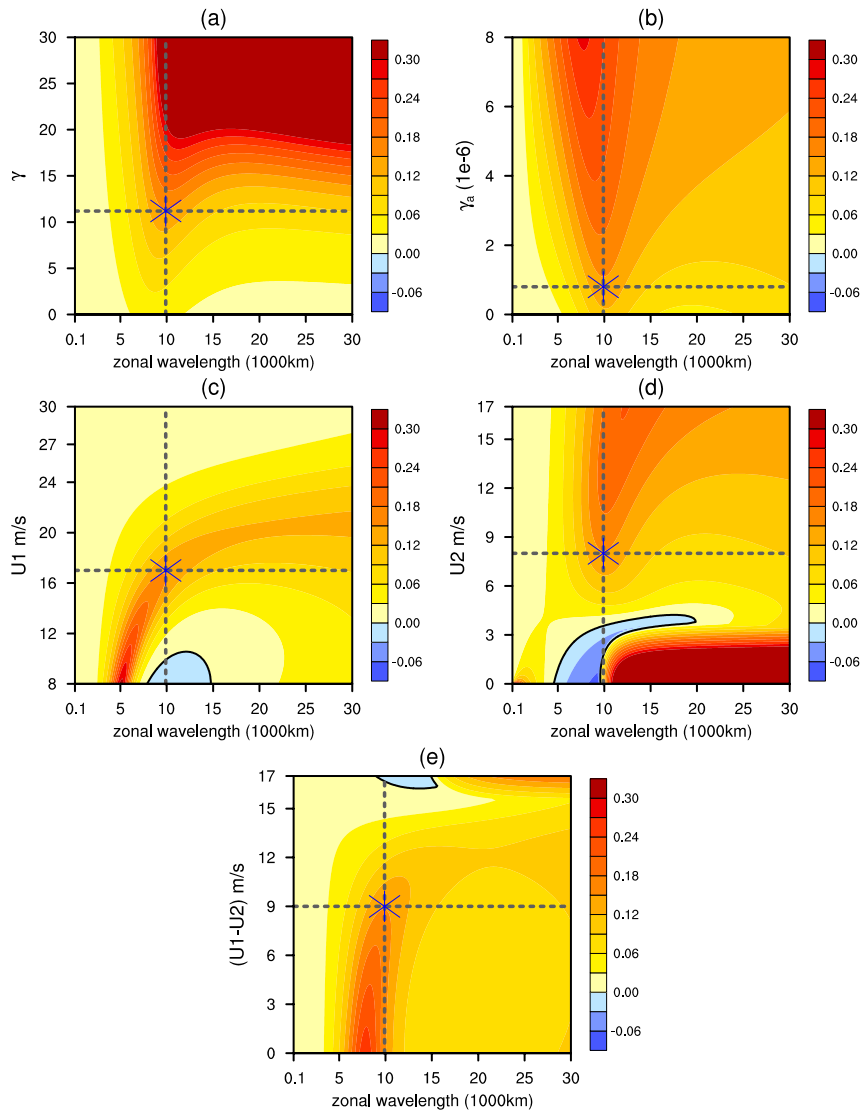


902

903 **Figure 12.** Growth rate as a function of wavelength for the coupled oceanic Rossby  
904 wave mode with (a) full oceanic processes in SST evolution equation, (b)  
905 entrainment- process only, and (c) advection process only. Note that (a) is the same as  
906 Fig. 3b.

907

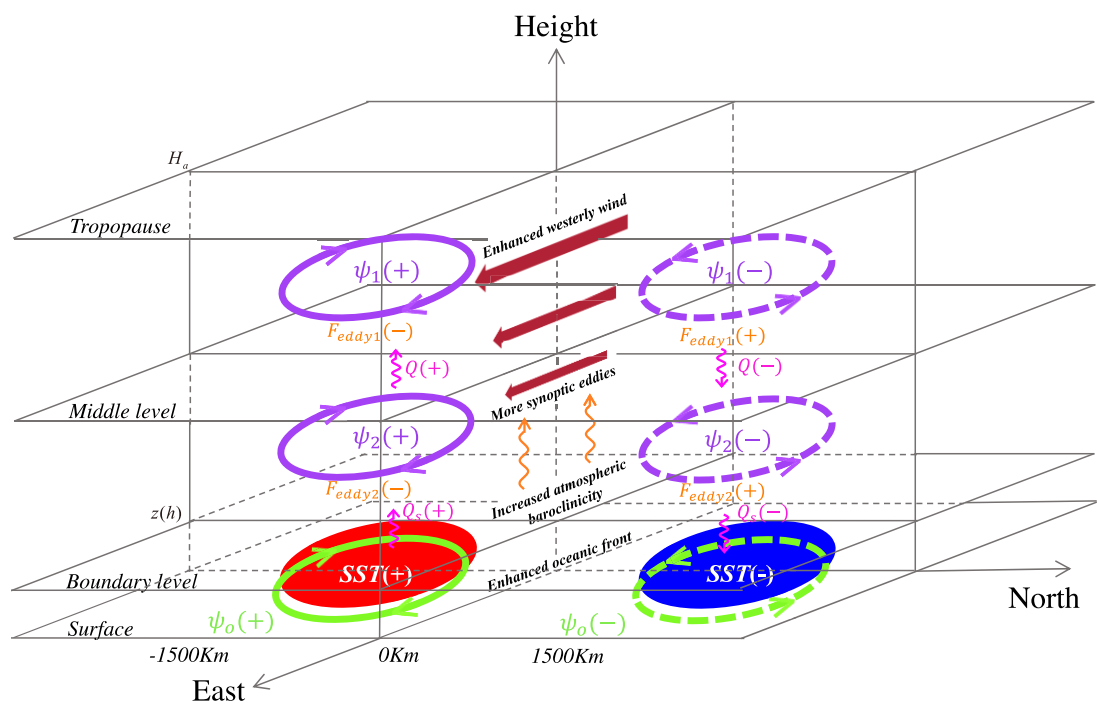
908



910

911 **Figure 13.** Unstable growth rate of coupled oceanic Rossby wave mode as a function  
 912 of zonal wavelength versus (a) dynamical coupling coefficient ( $\gamma$ ), (b) thermal  
 913 coupling coefficient ( $\gamma_a$ ), (c) the higher-layer background zonal wind ( $U_1$ ), (d) the  
 914 lower-layer background zonal wind ( $U_2$ ) and (e) the vertical wind shear ( $U_1 - U_2$ ),  
 915 respectively.

916



917

918 **Figure 14.** Schematic diagram of the phase relationships among atmospheric and  
 919 oceanic variables for the most unstable coupled oceanic Rossby wave mode in the  
 920 midlatitudes.

921

922

# Figures

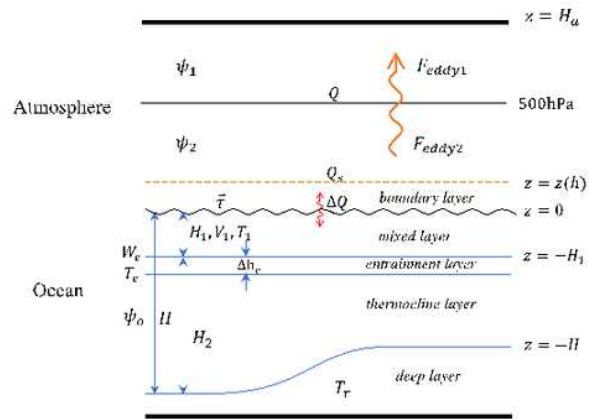
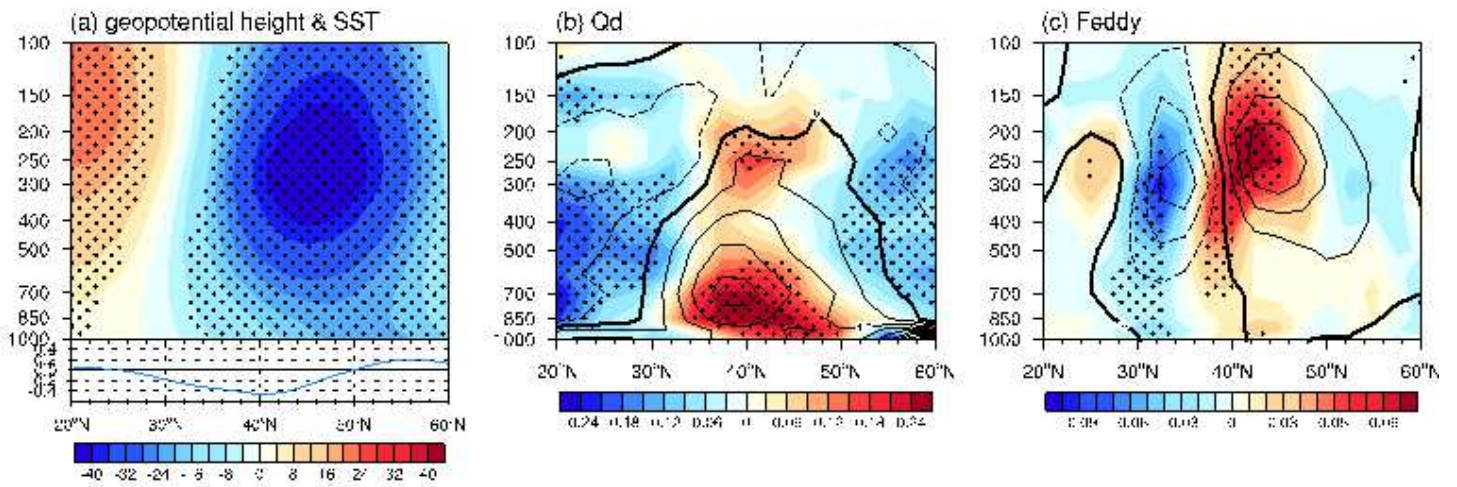


Figure 1

See the Supplemental Files section for the complete figure caption



**Figure 2**

See the Supplemental Files section for the complete figure caption

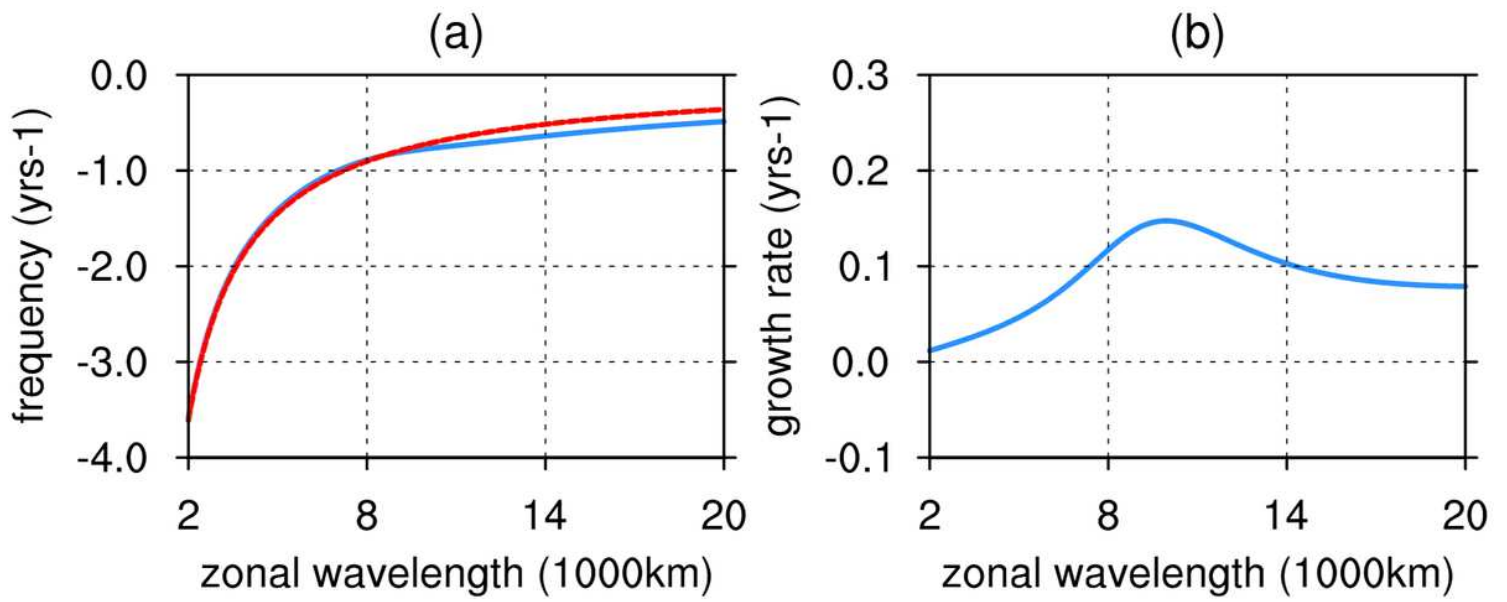
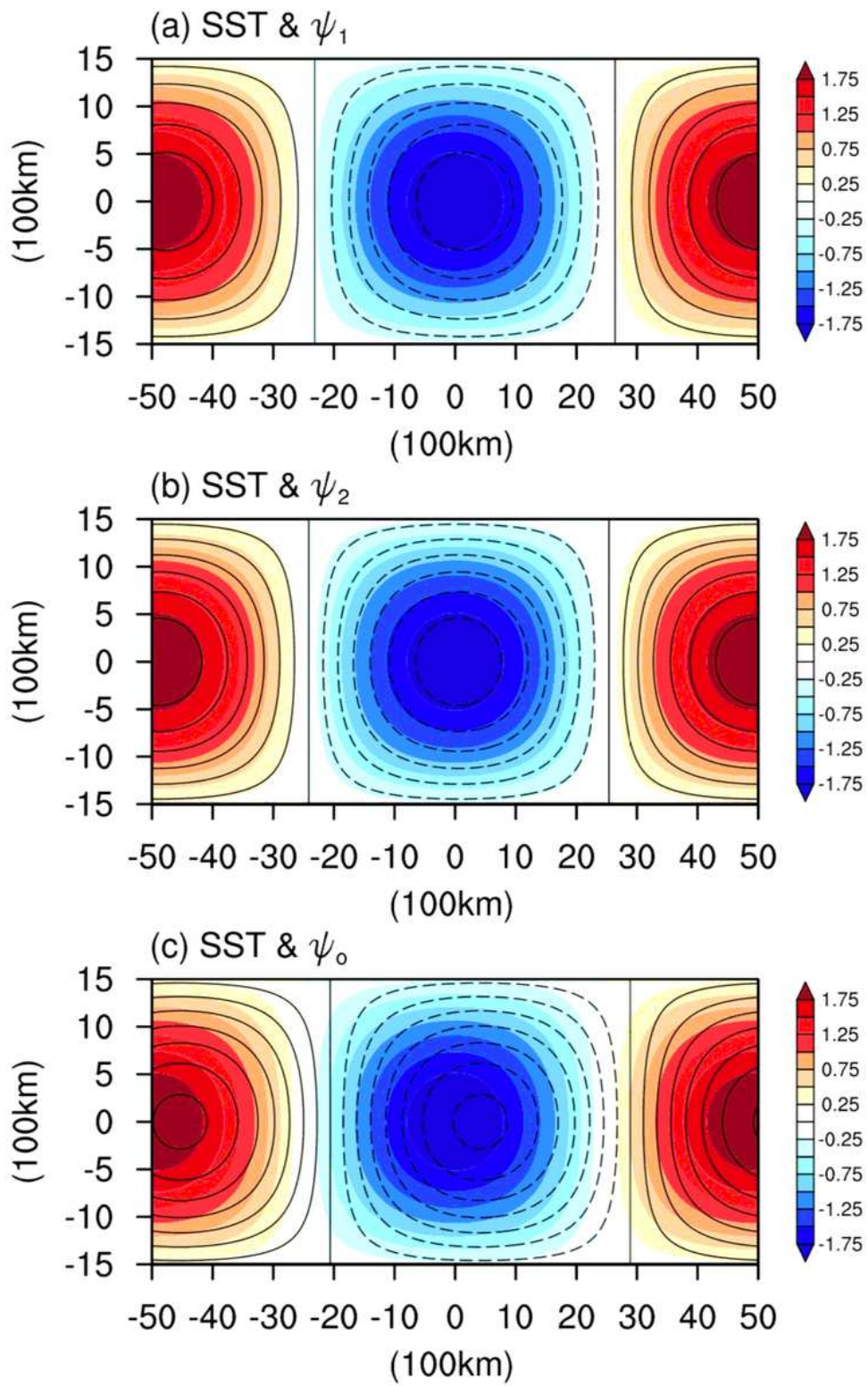


Figure 3

See the Supplemental Files section for the complete figure caption



**Figure 4**

See the Supplemental Files section for the complete figure caption

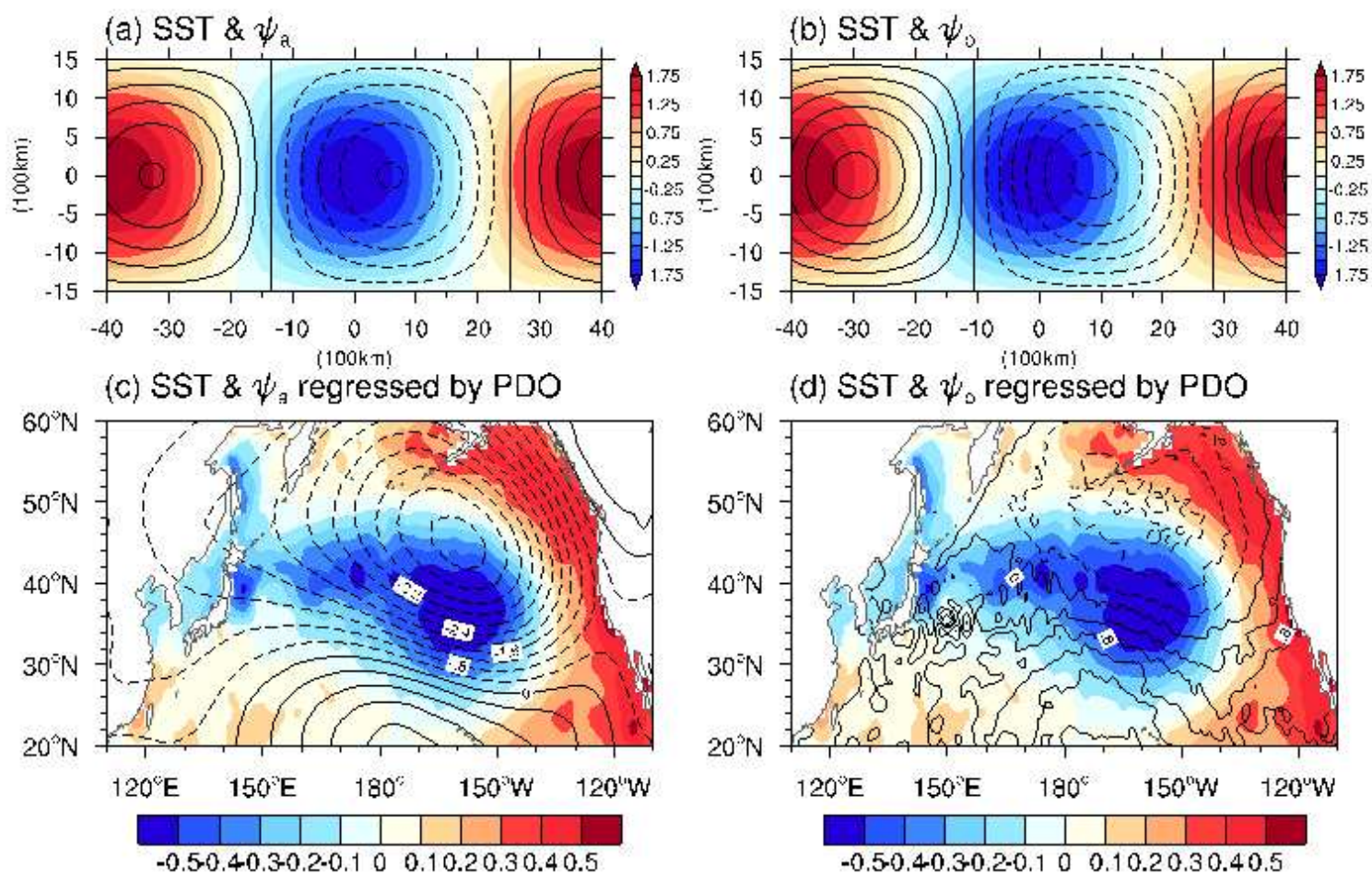


**Figure 5**

See the Supplemental Files section for the complete figure caption

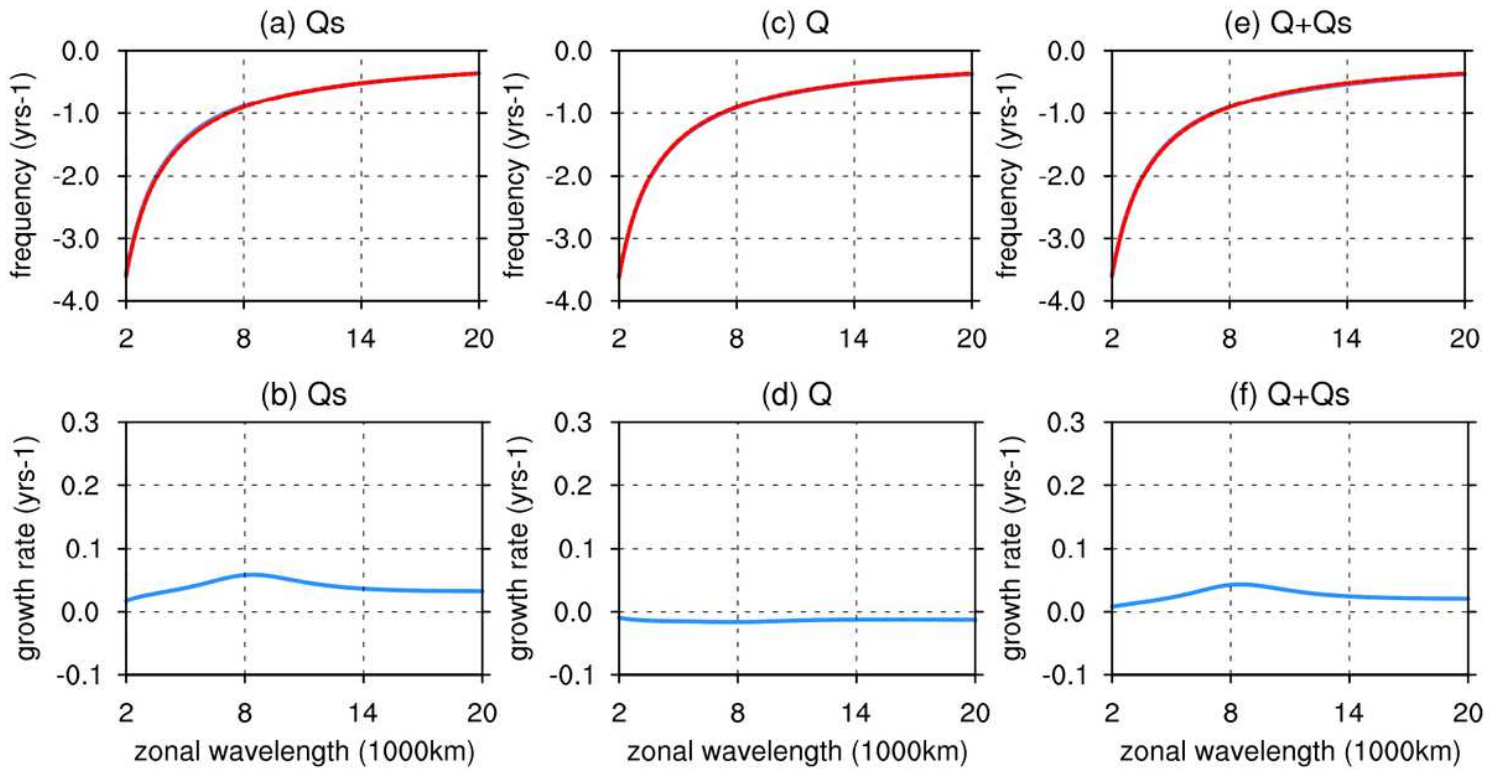


**Figure 6**

See the Supplemental Files section for the complete figure caption

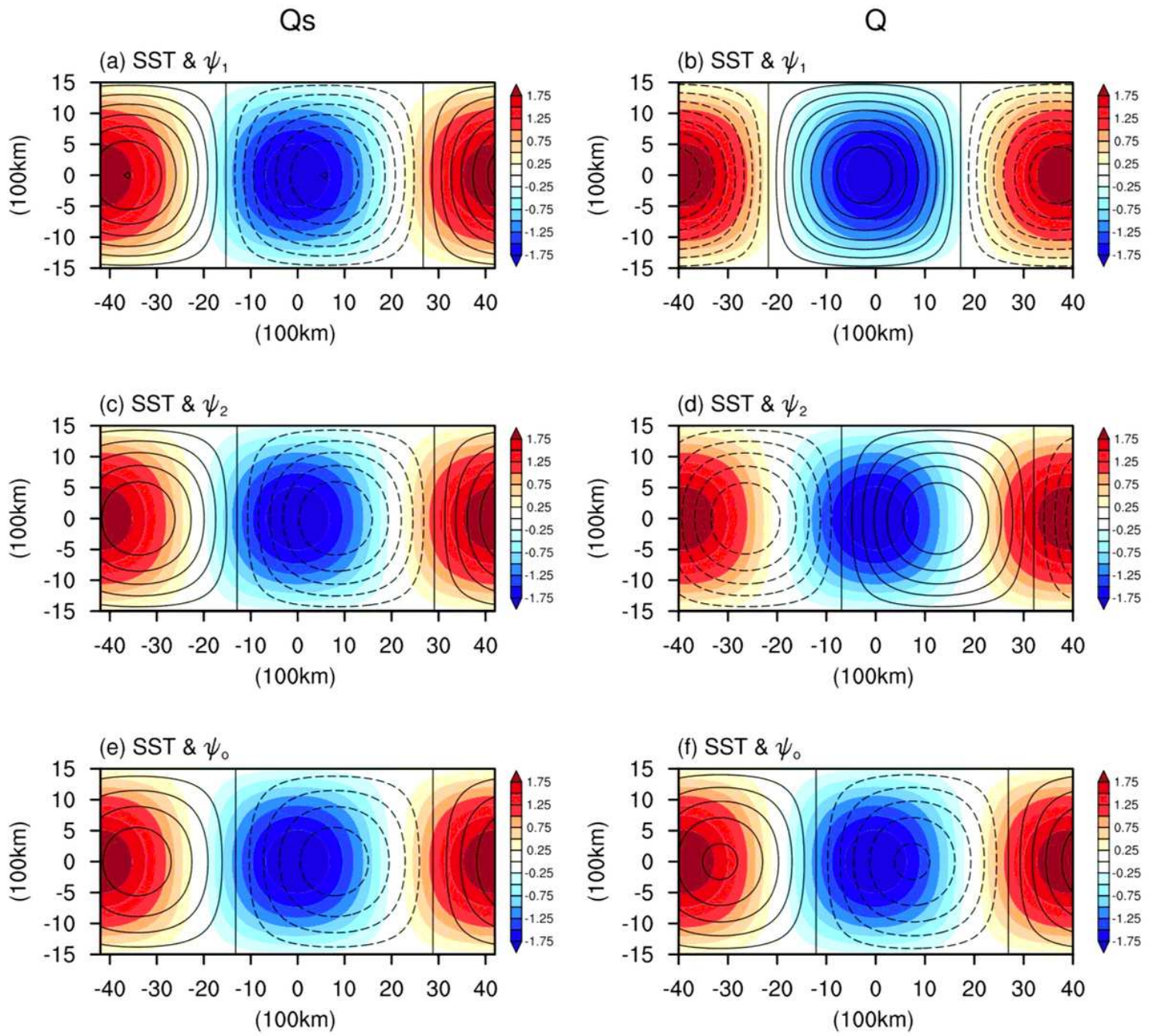


**Figure 7**

See the Supplemental Files section for the complete figure caption

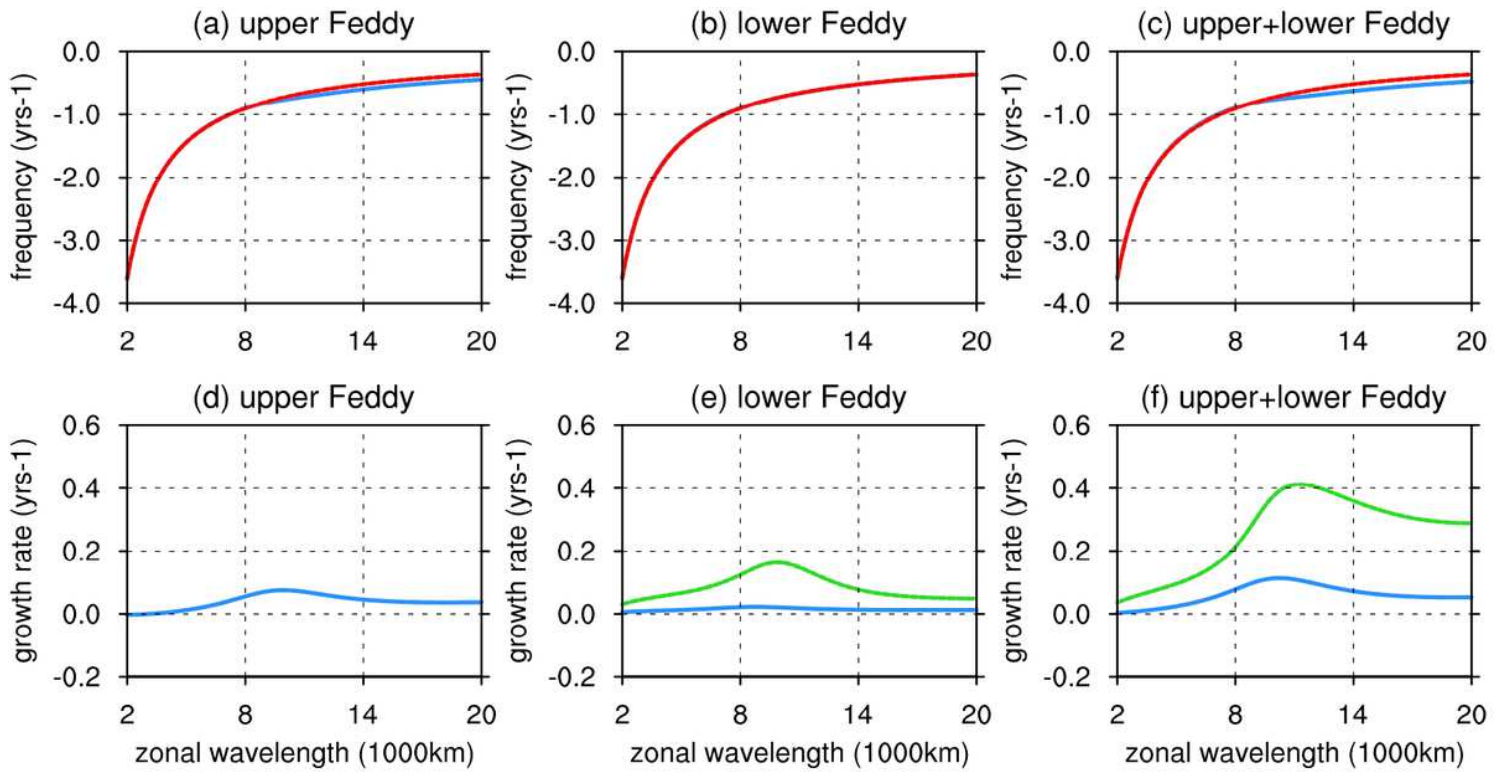


**Figure 8**

See the Supplemental Files section for the complete figure caption

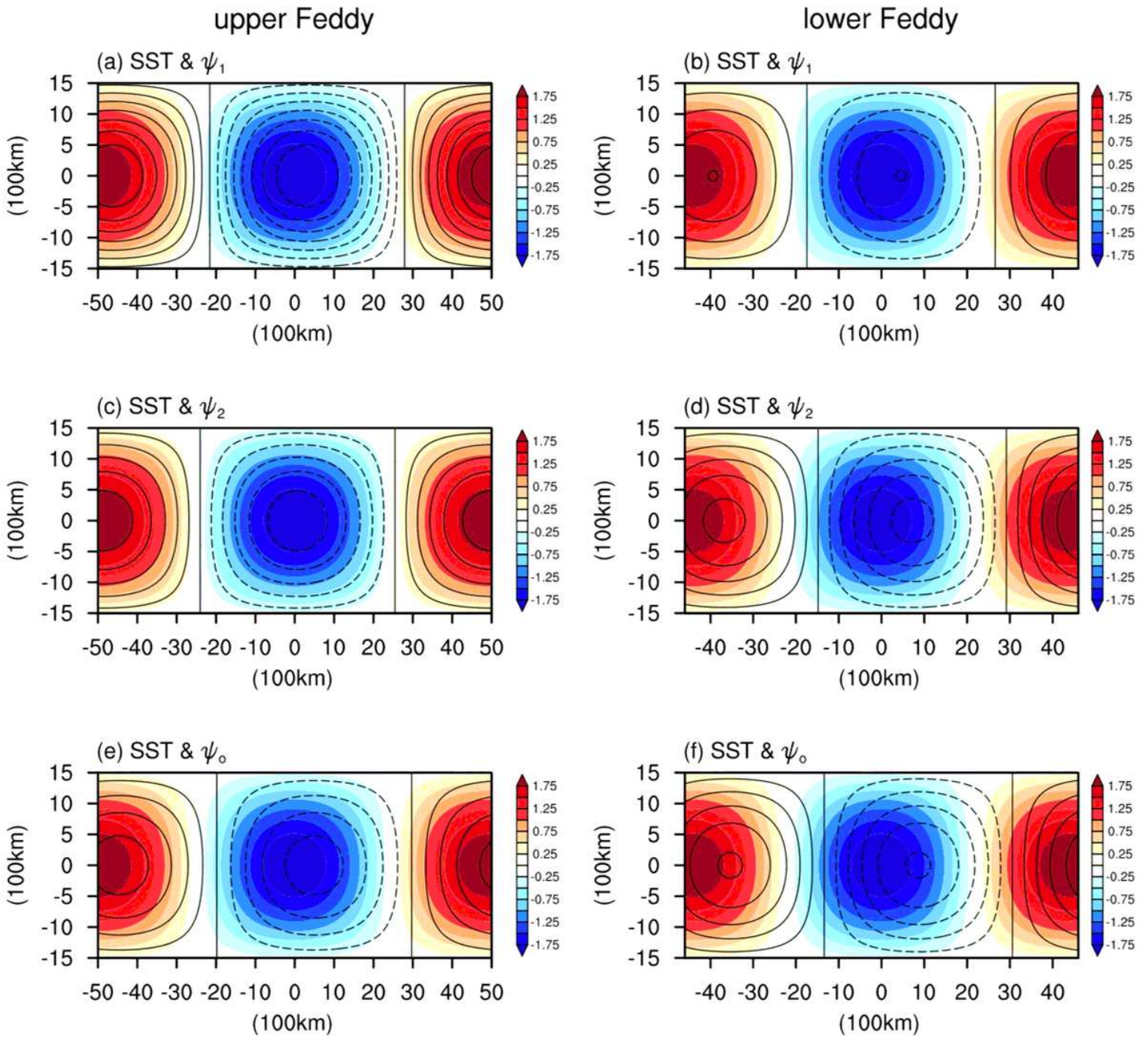


**Figure 9**

See the Supplemental Files section for the complete figure caption

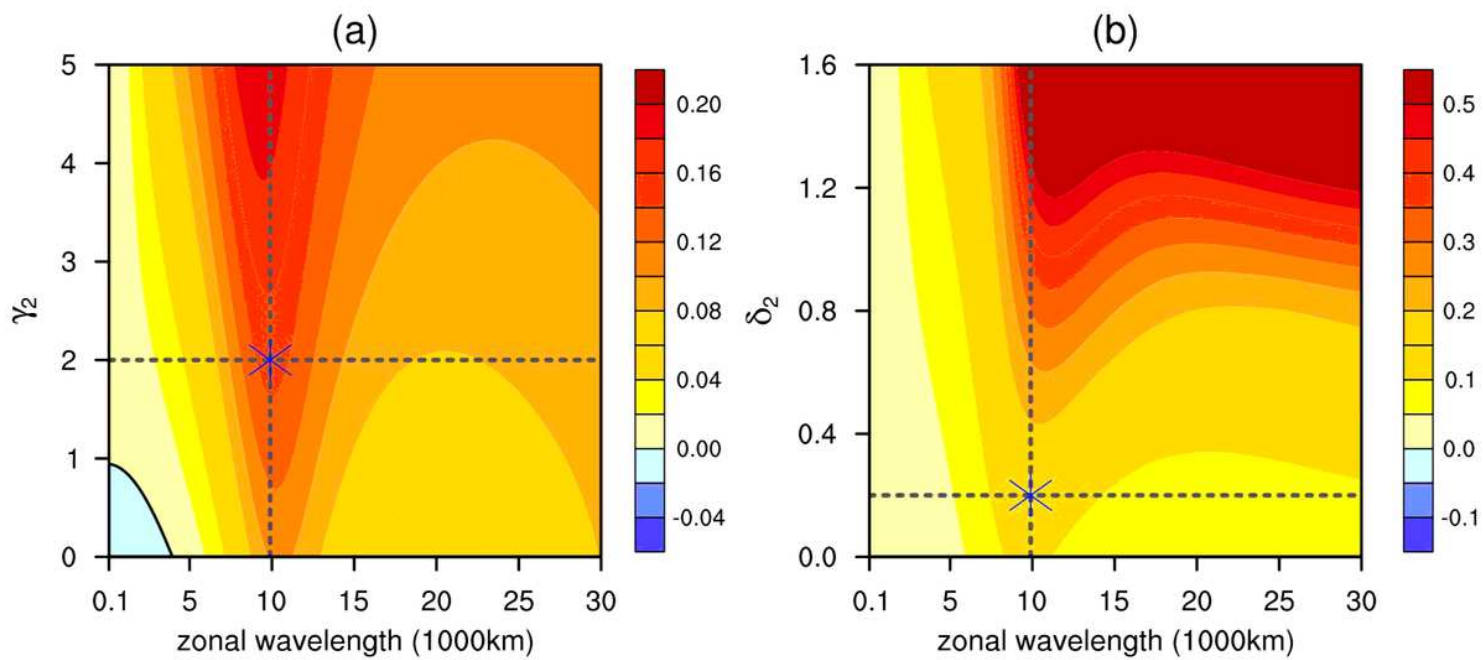


**Figure 10**

See the Supplemental Files section for the complete figure caption

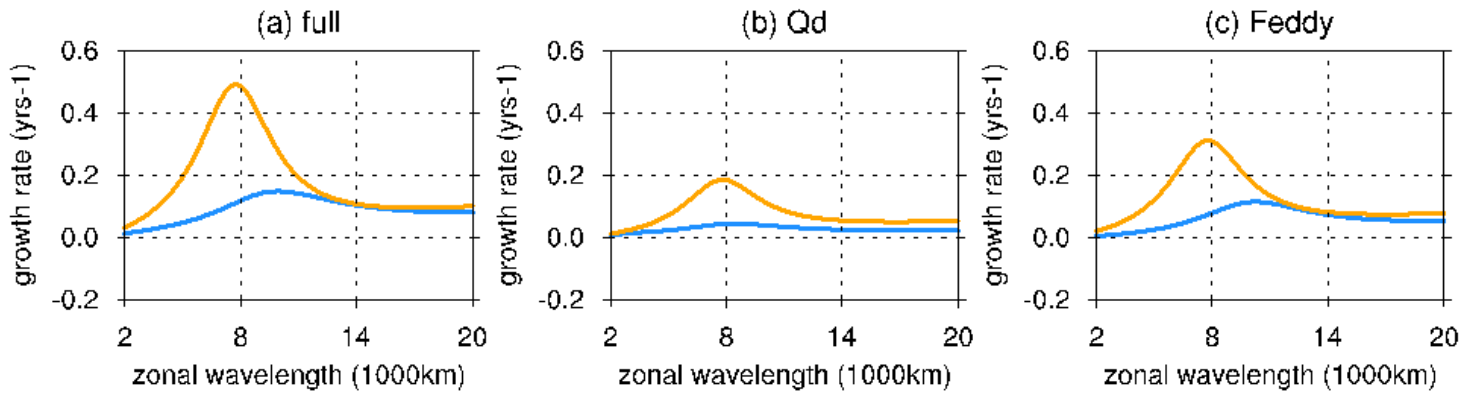


**Figure 11**

See the Supplemental Files section for the complete figure caption

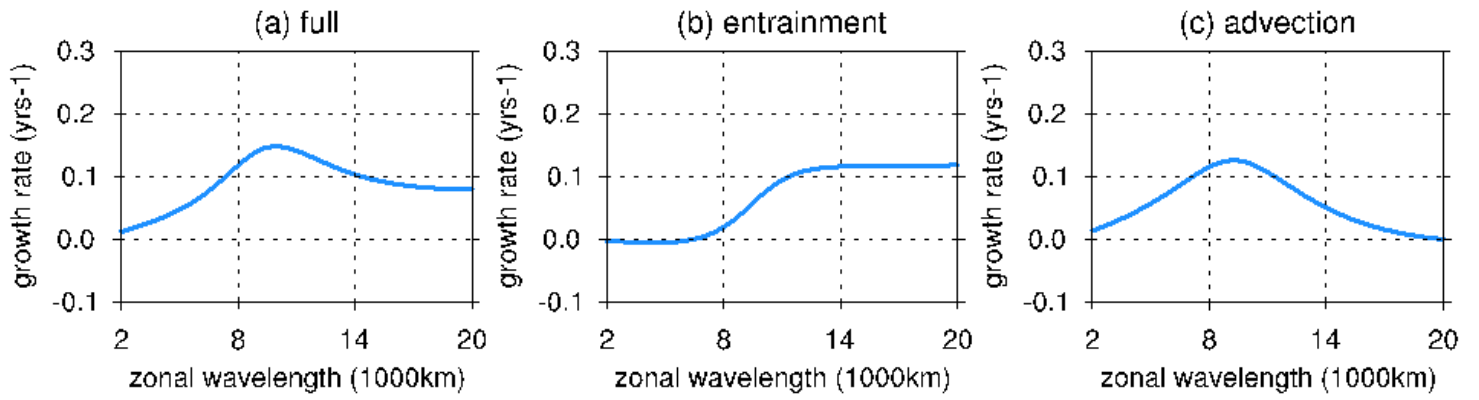


**Figure 12**

See the Supplemental Files section for the complete figure caption

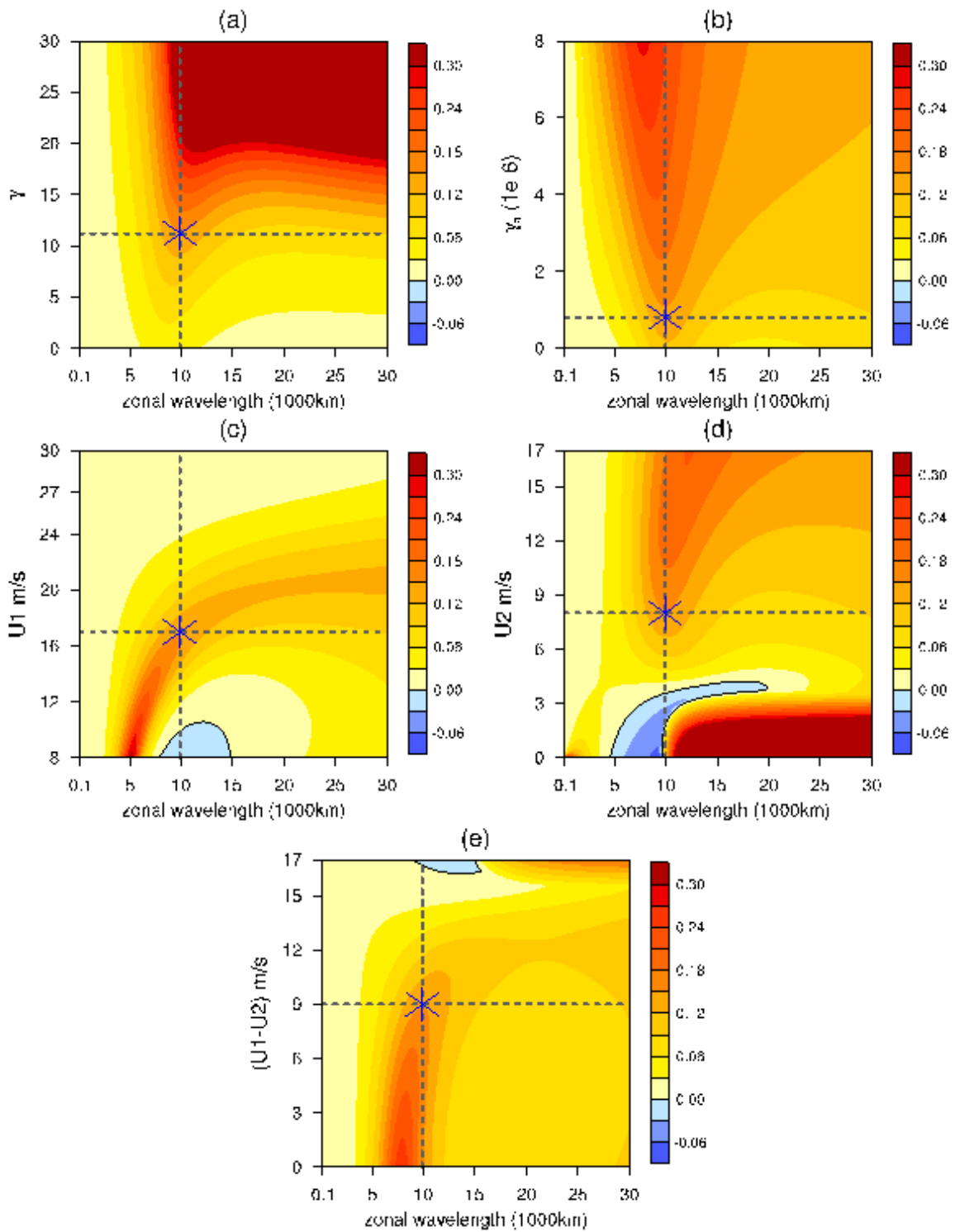


**Figure 13**

See the Supplemental Files section for the complete figure caption

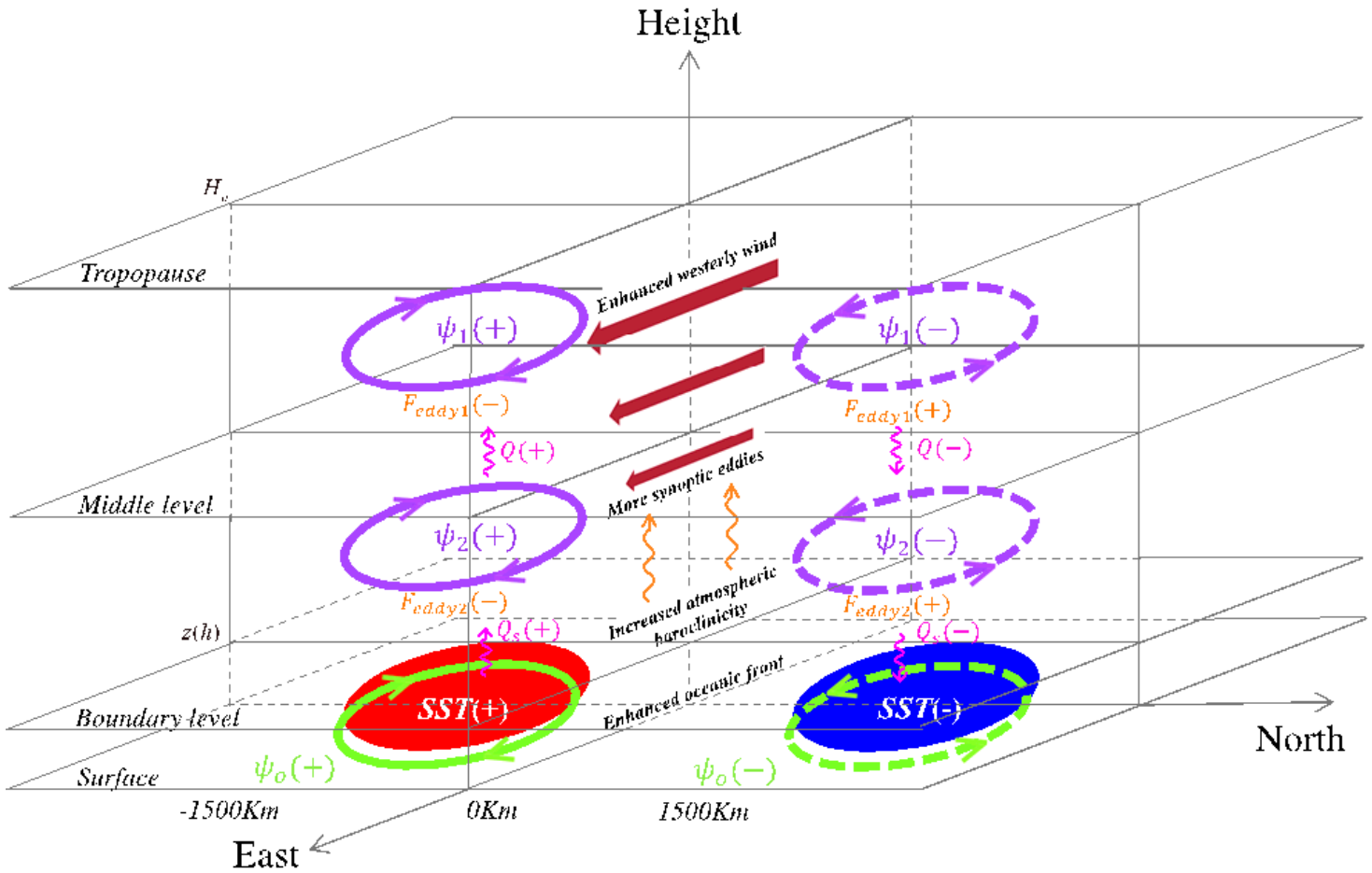


Figure 14

See the Supplemental Files section for the complete figure caption

## Supplementary Files

This is a list of supplementary files associated with this preprint. Click to download.

- [FigureCaptions.docx](#)